Chapter 7

Line Feed Implementation and Evaluation

Although a feed design was presented in Chapter 6, experimental measurements are required to evaluate the in-pairs feeding technique, the effect of the balun on the radiation performance and array performance, and to validate the simulation models. This chapter describes the detailed implementation, array measurement and evaluation of the wideband dipole design.

Section 7.1.1 describes the cable balun fed element, used to validate the in-pairs feeding technique and the simulated element patterns. Difficulty in element construction, alignment and impedance matching inflexibility for the cable-fed element lead to the design of a microstrip-fed element presented in Section 7.1.2. An estimation of feed losses for a single microstrip-fed element is presented in Section 7.1.3. An 8-element microstrip-fed module was measured for the pattern performance presented in Sections 7.2.1 and 7.2.2 and the impedance performance in Section 7.2.3. An aperture efficiency analysis described in Section 7.3 evaluates the measured feed radiation performance for the MOST reflector. Section 7.4 presents a grating lobe analysis, which investigates their influence on the line feed scanning performance.

7.1 Feed Prototype

This section describes the experimental implementation of the in-pairs feeding technique for the wideband dipole element shown in Figure 6.3. Fixed parameters in the element design, seen in Figure 7.1, are the arm width 114.3 mm ($0.3\lambda_c$), arm height 86.6 mm ($0.25\lambda_c$) and the arm gap 3 mm ($0.009\lambda_c$) where λ_c is the wavelength at the centre frequency 866 MHz. The dipole arms were constructed as copper metallisation on a circuit board, which is called the arm board. Metallised arms were printed on both sides of the arm board, which were connected together using plated through holes or vias as shown in Figures 7.2 and 7.5. This was done to minimise the effect of the dielectric substrate on the electrical performance of the feed.

The gap between the dipole arms was selected as 3 mm to minimise the feed balun connection distance across the arms. A large gap would result in increased inductance, which would be difficult to tune out and could generate resonances in the input impedance. However, there is a compromise because a small gap degrades the radiation and impedance performance of the feed. A balun was used to generate the voltage across the dipole arms because it minimises feed losses, as described in Section 4.1.2. A combining network printed on a baseboard, placed 0.25λ below the dipole arms, connects a pair of balun outputs to facilitate the in-pairs feeding technique. Low noise amplifiers (LNA) are then placed directly after the combining network, for each polarisation, to

maximise signal-to-noise performance. Cable and microstrip baluns were designed in the prototype stages, in order to evaluate various aspects of the wideband dipole design and construction. These designs are described in Sections 7.1.1 and 7.1.2 respectively.

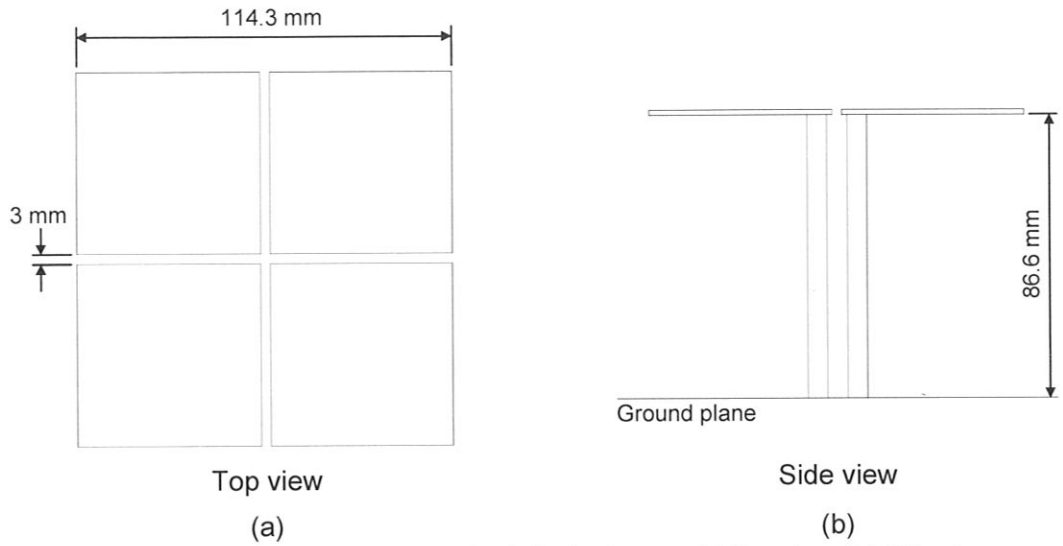

Figure 7.1 Wideband dual polarised dipole element. (a) Top view. (b) Side view.

7.1.1 Cable Balun Design

A cable balun, shown in Figure 6.4, feeds the wideband dual polarised dipole to test the in-pairs feeding technique concept and to compare measured element patterns with simulated results from Chapter 6. Cables to feed the dipole enabled a simple and cheap construction, using a semi-flexible 0.141 inch 50 Ω microwave cable known as SM141 (www.hubersuhner.com). The prototype is shown in Figure 7.2 and consists of an arm board, four cable baluns and a baseboard. The arm board is a printed circuit board (PCB) with metallised dipole arms and the baseboard uses an FR4 dielectric substrate with a printed combining network to facilitate the in-pairs feeding for both horizontal and vertical polarisations. The electrical and mechanical specifications of the FR4 dielectric substrate are contained in Table 7.1.

Parameter	Specification
Material type	FR4 Substrate
Dielectric constant	4.6 ± 0.3
Loss tangent (tanδ)	0.02
Board thickness	1.6 mm
Copper (Cu) cladding	1 oz. (35 μm) electrodeposited Cu foil

Table 7.1 Parameters of the FR4 substrate used for the arm board and baseboard.

Each balun uses two cables approximately 86.6 mm ($0.25\lambda_c$ at 866 MHz) in length, which are connected across different arms. For example, the single dipole B-D is fed by balun 4 as shown in Figure 6.4. The balun has the outer conductor of one feed cable soldered to the ground layer of the baseboard located at the ground plane. The outer conductor at the opposite end of the cable is soldered to arm D, on the arm board. The inner conductor of the feed cable is connected to its neighbouring arm, B, along the arm width dimension. The balun is completed by using a second cable to electrically connect arm B to the ground plane, to balance the currents on the outer conductor of the feed

cable connected to arm D. This is done by connecting the outer conductor of the cable to the baseboard ground layer and the opposite end to arm B on the arm board. Each pair of baluns with the same polarisation orientation are connected to a pair of equal length microstrip lines connected to a common feed point on the baseboard, to provide the in-pairs feeding. Thus there are eight cables connected to the line feed element.

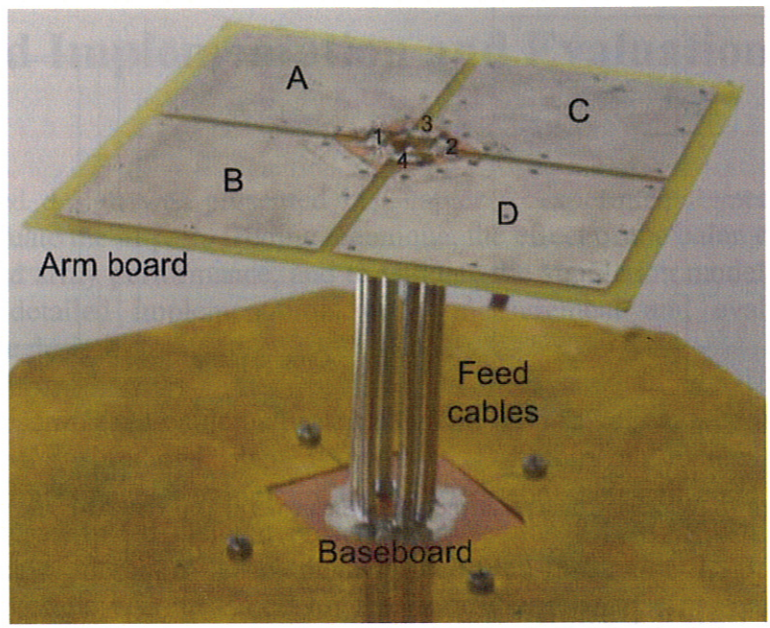

Figure 7.2 Prototyped cable-fed wideband dual polarised line feed element.

The measured return loss of a single element was around –8 dB across the 700–1000 MHz band. No attempt was made to improve this result at this stage. The goal was to validate the in-pairs feeding technique by comparing measured and simulated element patterns. A single channel 4-element line feed, with channel dimensions: 200 × 40 mm, was constructed and transverse and longitudinal plane element patterns were measured at the Argus Technologies ground reflection antenna testing range, using a procedure to be described in Section 7.2. Good agreement between measured and simulated transverse element patterns is seen in Figures 7.3 and 7.4, at 0° scan angle for vertical and horizontal polarisations. The next stage of the design was to improve the impedance performance, to attain a –10 dB return loss, using a matching network. A matching network must be placed after the in-pairs connection on the baseboard rather than integrating it with the cable balun because the fixed 50 Ω impedance of the feed cables offers limited tuning capability.

In addition to providing the balun feed, the cables give physical support and alignment for the arm board as shown in Figure 7.2, but the semi-flexible SM141 cables made construction and alignment difficult. For increased stability semi-rigid cables were used, but the increased heat to solder them onto the boards resulted in the metallisation peeling from the substrate. The dielectric inside the cable expanded making it difficult to construct and maintain alignment. Although a slight misalignment for the top board was acceptable in the prototyping and testing stages of the cable-fed design, an alternative design using a microstrip balun was desirable for the next stage of the feed development.

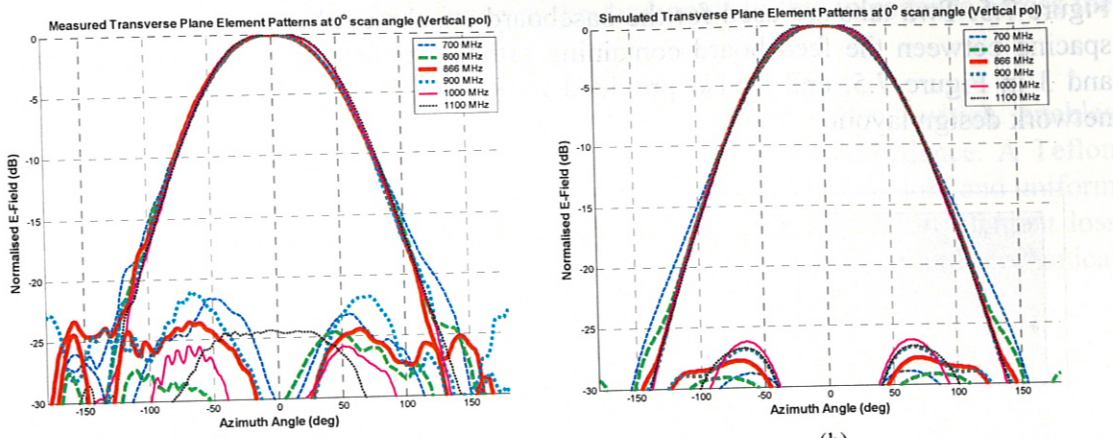

(a) (b)

Figure 7.3 Vertical polarisation co- and cross-polar transverse plane element patterns for a 4-element array across 700–1100 MHz at 0° scan angle. (a) Measured. (b) Simulated.

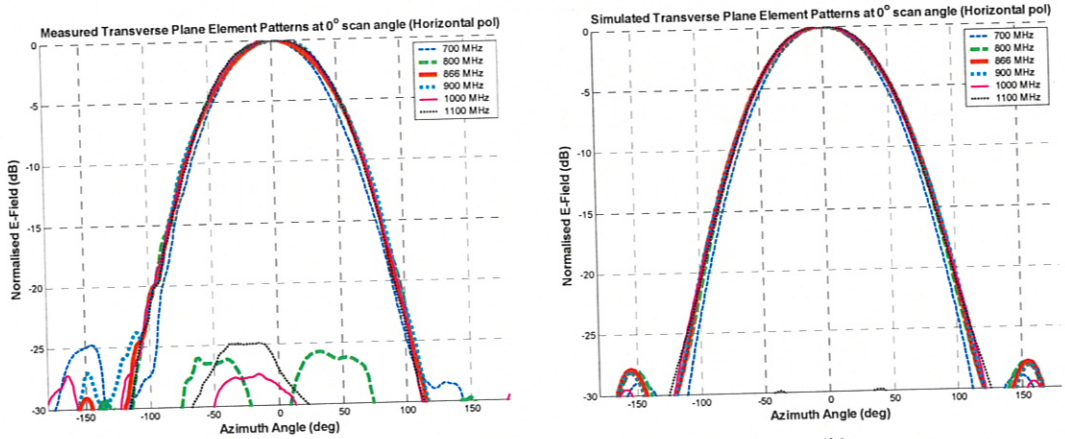

(a) (b)

Figure 7.4 Horizontal polarisation co- and cross-polar transverse plane element patterns for a 4-element array across 700–1100 MHz at 0° scan angle. (a) Measured. (b) Simulated.

7.1.2 Microstrip Balun Design

The operating principle for the microstrip balun is similar to the cable balun, except that a different transmission medium is used. The primary difference is that the ground plane side of the microstrip board replaces the outer conductor of the feed cable and the printed track on the microstrip board replaces the inner conductor of the cable. Four different microstrip feed boards replace the eight cables, with the arm board and baseboard remaining the same. The new method of assembly is shown in the side view of Figure 7.5. The arm board, in the top view of Figure 7.5, has four diagonal slots near the feed point of each arm which enables the attachment of the four microstrip feed boards. The slot dimension was chosen to minimise the balun feed connection distance on the arm board, reducing the effect of the feed inductance and resonances on the input impedance. Each microstrip feed board has a top tab, shown in the microstrip feed board view in Figure 7.5, with a width that matches the diagonal slot dimensions on the arm board. Each feed board can be inserted into the corresponding slot in the arm board and then soldered in place. This construction technique improves the alignment of the arm board and element stability. A similar technique was used for the baseboard. Attachment of the four feed boards required eight diagonal slots in the baseboard, as shown in the bottom view of

Figure 7.5. Two tabs are used for the baseboard attachment because it allowed a greater spacing between the feed board containing orthogonal feed tracks, labelled as tracks 2 and 3 in Figure 7.5, and it also provided more flexibility in the baseboard combining network design layout.

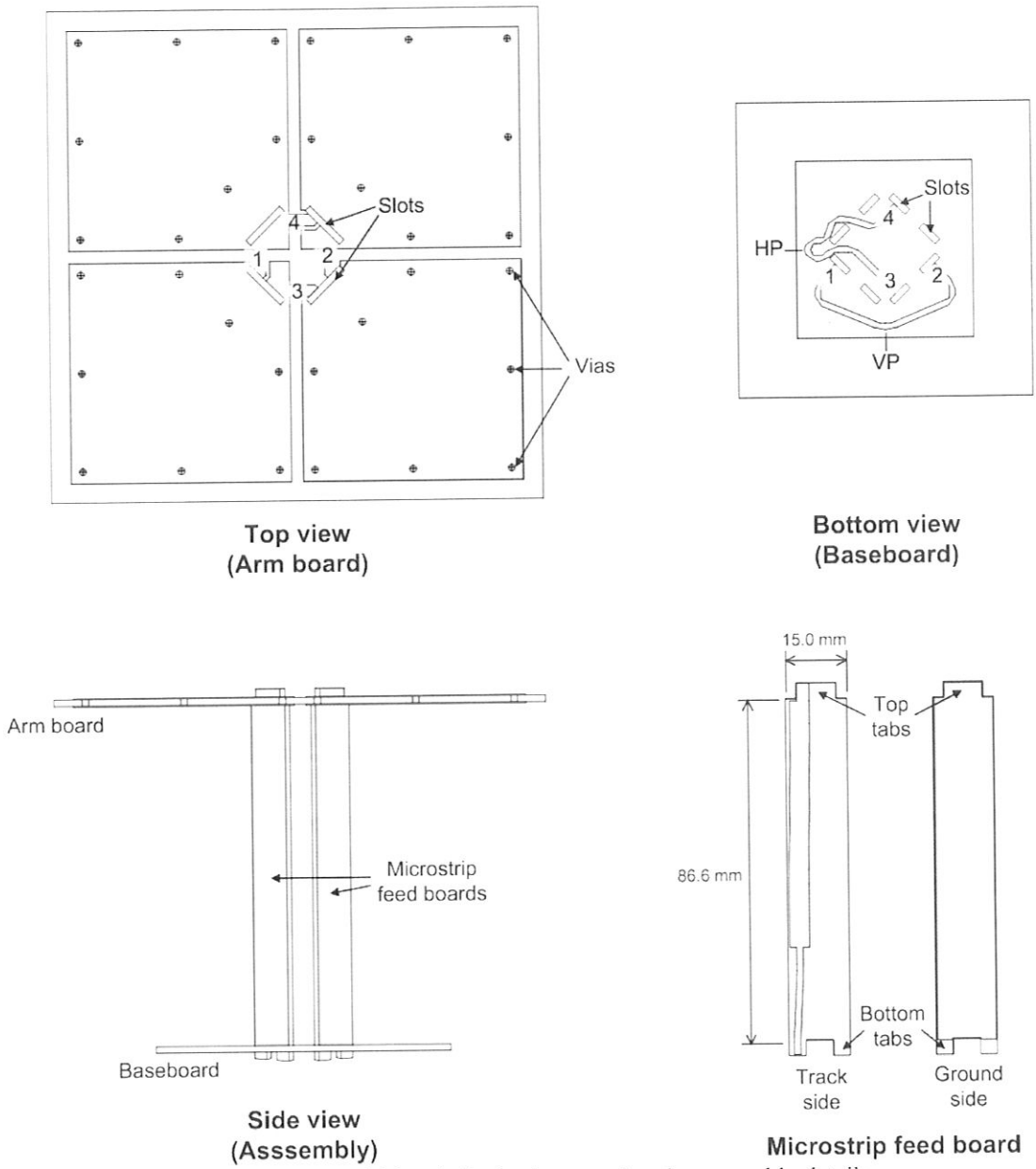

Figure 7.5 Wideband dipole element, showing assembly details.

The baseboard design, shown in the bottom view of Figure 7.5 consists of two combining networks to provide the equal-amplitude, equal-phase feeding for horizontal and vertical polarisations. Unbalanced outputs from a pair of microstrip baluns having the same polarisation orientation were connected to a single feeding point. For vertical polarisation, outputs from tracks 1 and 2 are combined at point VP and similarly, outputs from tracks 3 and 4 are combined at point HP for horizontal polarisation. The respective combining points for both polarisations are where the first-stage LNAs are connected. The input impedance specified for the LNA used in this design is 50 Ω so a matching network was

designed to match the antenna impedance at the feed point to this impedance across the 700–1000 MHz band.

The matching network was integrated into the microstrip balun, which enables modification of the feed track width as a means of changing the impedance. A Teflon substrate was chosen for the microstrip board design, because of its low loss and uniform dielectric constant across the required frequency range. This enabled low element loss and accurate design of the impedance matching network. The electrical and mechanical parameters of the substrate are listed in Table 7.2 (Neltec Datasheet 2006).

Parameter	Specification
Material type	Neltec Teflon substrate NX9255
Dielectric constant (ε_r)	2.55 ± 0.04 (10 GHz)
Loss tangent (tanδ)	0.0018 (10 GHz)
Board height	1.524 mm
Copper (Cu) cladding	1 oz. (35 μm) electrodeposited Cu foil

Table 7.2 Parameters of the Teflon substrate for the matching network.

Initially the antenna impedance at the feed point was obtained using the model described in Section 6.4.5. This determines the type of matching network required. Other parameters that influenced the design were the practical maximum and minimum track widths, which were determined using the software package txline 2003 (AWR 2006).

The width of the feed board, shown in the microstrip feed board view of Figure 7.5, is selected to be 15 mm, to minimise the feed track distance on the arm board and to provide sufficient mechanical support and alignment for the arm board. The dual polarised in-pairs feeding technique requires one of the four microstrip feed boards to contain two printed feed tracks, to connect to feed tracks 2 and 3 shown in the arm board view in Figure 7.5. The two feed tracks must be spaced so that coupling between them is minimised. A consequence of insufficient spacing includes generating an out-of-phase excitation, which produces asymmetric transverse line feed patterns. A maximum track width of 6.5 mm was set for the 15 mm wide feed board. This width permitted a gap of at least 2 mm between the two tracks as shown in Appendix C, Figure C.2(a). A 6.5 mm track width corresponds to a 37 Ω impedance at the design frequency, 866 MHz, using the Teflon substrate. The minimum track width is determined experimentally. Thin feed tracks are prone to lift off the substrate when soldered and are difficult to work with when trying to obtain accurate impedances in the prototyping stages. From previous experience with the same substrate, the minimum usable track width is 1.5 mm, which corresponds to an 89 Ω impedance at 866 MHz. Hence, the range of impedance available for the feed board matching network was 37–89 Ω, subject to the track width constraints in the range 1.5–6.5 mm.

Using the model described in Section 6.4.5, the impedance at the antenna feed point at 866 MHz was calculated to be $Z_A = 23.0 + j0.8$ Ω. The Smith chart in Figure 6.28 shows the largest reactance across the 700–1000 MHz range is around –j13 Ω at 700 MHz. A possible network that could be to used match Z_A to the 50 Ω LNA input impedance is a quarter-wave transformer and the –j13 Ω capacitive reactance can be tuned out by the series inductance at the feed point generated by the feed section shown on the arm board in Figure 7.5. The series inductance at the feed point in Figure 7.5 is not represented as a typical electronic component. Rather, it is physically represented as a microstrip feed tab

in the microstrip feed board view and also as a length of feed track connecting the arms together near the slots for each pair of dipoles in the top view. There will also be additional series inductance from the amount of solder used to connect the microstrip feed board tabs to the top board.

Equation 7.1 was used to calculate the impedance of the quarter-wave transmission line.

$$Z_{QW} = \sqrt{Z_L Z_{in}} \tag{7.1}$$

Where Z_{QW} = quarter-wave transformer impedance
Z_L = load impedance
Z_{in} = input impedance

In the quarter-wave matching network design, Z_L was the antenna impedance at the centre frequency, $Z_A = 23.0 + j0.8\ \Omega$, and the input impedance, Z_{in} was the LNA impedance, 50 Ω. Using these parameters, the impedance of the quarter-wave transmission was calculated as $Z_{QW} = 34\ \Omega$, which corresponded to a 7.3 mm track width and a 58.3 mm length ($0.25\lambda_c$ at 866MHz). This impedance is outside the range of impedances available for the feed network and a single quarter-wave matching network would result in a 0.4 mm gap between feed tracks on the microstrip board with two feed tracks, which would cause increased coupling. To minimise the width of the feed track, and increase the gap between the feed tracks, a two-stage quarter-wave transformer matching network, shown in Figure 7.6, was used. This network enabled the impedances selected for the design to remain within the 37–89 Ω limits. The first stage quarter-wave transformer, T_{L1} was designed to match to an arbitrary impedance, Z_B, at point B such that the impedance of the transformer Z_{QW1} was within the range of acceptable impedances. The impedance Z_B was chosen to be 100 Ω, which required a quarter-wave matching network T_{L1} with $Z_{QW1} = 48\ \Omega$, corresponding to a 4.5 mm track width and a 59.3 mm length. In the second stage, a quarter-wave transformer T_{L2} was required to match the impedance at point B, $Z_B = 100\ \Omega$ to the LNA impedance at point C, $Z_{LNA} = 50\ \Omega$. The impedance for the second-stage quarter-wave transformer was calculated to be: $Z_{QW2} = 70.7\ \Omega$, corresponding to a 2.4 mm track width and a 60.6 mm length. A Smith chart with arrows illustrating the transformation of the antenna impedance, Z_A, at different points in the matching network is shown in Figure 7.7, with the cross (×) representing the 50 Ω impedance point.

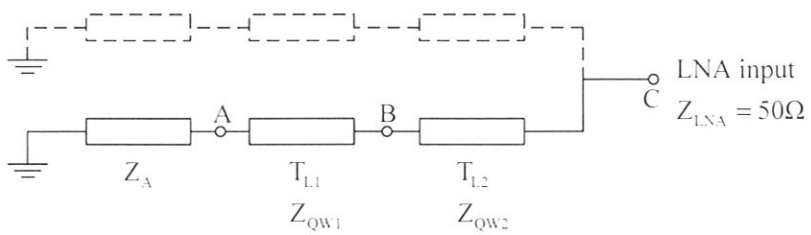

Figure 7.6 Circuit diagram of the two-stage quarter-wave transformer matching network.

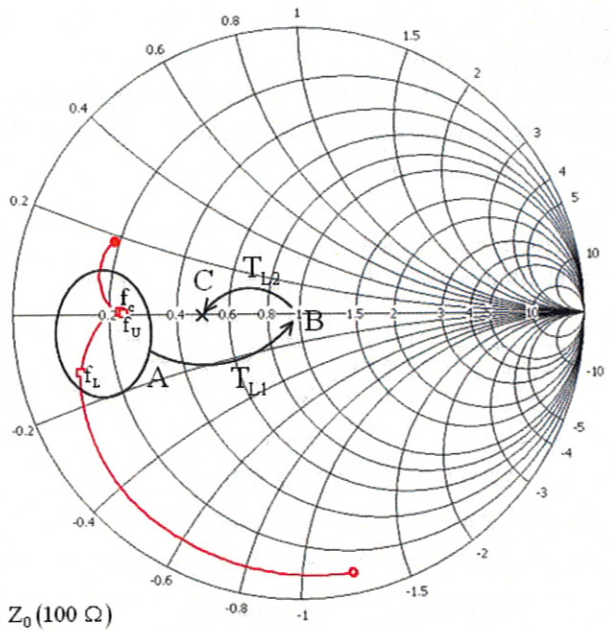

	Freq (MHz)	R (Ω)	X (Ω)
○	500	9.8	−122.0
f_L	700	11.9	−13.0
f_c	866	23.0	0.8
f_U	1000	24.0	0.3
●	1400	18.9	18.6

Figure 7.7 Smith chart of the antenna input impedance locus at the feed point. Arrows represent the impedance transformation at various points using the two-stage quarter-wave matching network from Figure 7.6. *Note the Smith Chart is referenced to 100 Ω, therefore the 50 Ω impedance circle is r = 0.5 (where: r = R/100), marked with a ×.

After the impedances for the two-stage matching network were obtained, layouts for the microstrip feed boards, arm board and baseboards were completed and sent out for manufacture. Testing of the matching network involved measuring the impedance of the assembled dipole element using a network analyser in an anechoic chamber at the Argus Technologies facilities. A single element was mounted on a 500 × 500 mm brass ground plane for the impedance measurements. In-pairs feeding for vertical and horizontal polarisation was generated by connecting 50 Ω cables to the points VP and HP shown in the baseboard view in Figure 7.5. After calibrating the network analyser to the test cable point, each polarisation was measured individually. A 50 Ω load was connected to the polarisation not under test.

Additional effects not included in the model are coupling between feed boards, fringing fields on the microstrip boards and inductance of the feed tabs on the arm board. Some experimental tuning was required to investigate if these effects produced any resonances in the antenna impedance. The aim is to minimise the return loss over the 700–1000 MHz band. Only the impedances on the Teflon feed board were modified. The impedance of the tracks on the baseboards was kept constant at the second-stage transformer impedance Z_{QW2} = 70.7 Ω. Modifications to the feed boards were made subject to the measured impedances at different reference planes along the matching network in Figure 7.6.

The complete experimentally tuned impedance matching network is shown in Figure 7.8. Differences between the calculated and experimentally determined impedances for the feed boards could be due to coupling between feed boards and microstrip fringing fields. The difference between calculated and experimental impedances for the baseboard, 70.7 Ω compared with 68.8 Ω, could be due to the ±0.3 dielectric constant variation in the FR4 substrate. The track length on the baseboard, T_3, was selected as $0.17\lambda_c$ (33 mm), which ensured a track length around $0.25\lambda_c$ was obtained when it was connected to the

partial second-stage quarter-wave feed track, T_2, on the Teflon feed board. The printed circuit board layouts for the matched wideband dipole are given in Appendix C, Figures C.1 to C.3. Microstrip feed boards were silver plated to reduce conductor loss and permit ease of soldering. The arm board and baseboard were plated with a thin layer of solder to enable ease of soldering and prevent copper oxidisation.

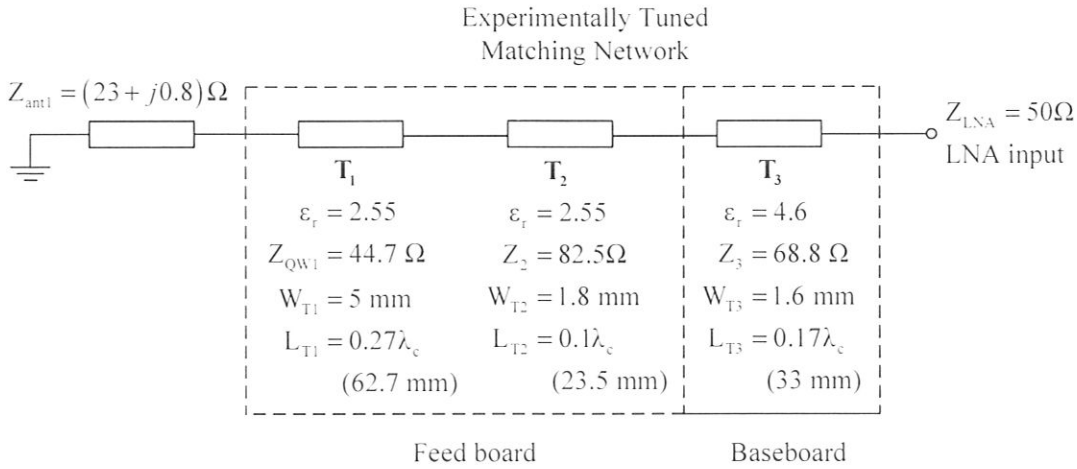

Figure 7.8 Experimentally tuned matching network transmission line parameters.

The impedance locus referenced to the input at the baseboard, LNA input, and return loss for vertical and horizontal polarisations are shown in Figures 7.9 and 7.10. The Smith Chart, shown in Figures 7.9(b) and 7.10(b), was used because it displayed impedances and provided information for matching the antenna across the frequency band. The impedance loci and return loss curves on both polarisations are relatively similar. Slight differences are attributed to the different baseboard track layouts. Results for the return loss and impedance at 700, 866 and 1000 MHz are listed in Table 7.3

Frequency (MHz)	Return Loss (dB)		Impedance (Ω)	
	Vertical pol	Horizontal pol	Vertical pol	Horizontal pol
700	–6	–6	26 – j38	29 – j41
866	–18	–20	39 + j3	48 + j7
1000	–16	–16	38 + j8	41 + j12

Table 7.3 Measured return loss and impedance of the wideband dipole prototype.

Table 7.3 shows that return losses at the lower frequency limit, 700 MHz, for both polarisations were outside the –10 dB specification. Measured results show the impedance locus (Figures 7.9(b) and 7.10(b)) in the frequency range from 866–1000 MHz is more inductive compared to the simulated results over the same range. This additional inductance comes from the inner conductor of the cable on the baseboard used to feed the antenna, which is not included in the simulation. The absence of sharp resonances in the impedance locus and return loss indicates the feed excitation was correct and there were no problems in the element construction due to coupling between feed tracks or inadequate electrical connection. Impedance measurements can be used to verify the correct element implementation, but element patterns are required to determine whether the microstrip balun design has an influence on the radiation performance. Measured element patterns are presented in Section 7.2.1 and 7.2.2.

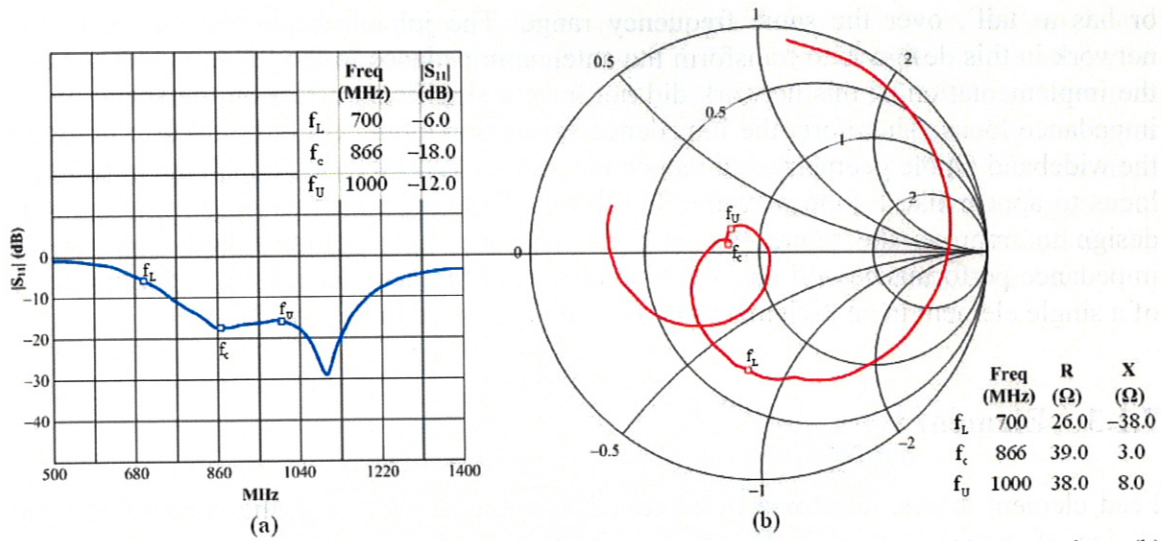

Figure 7.9 Measured vertical polarisation performance for single isolated element. (a) Return loss. (b) Impedance locus.

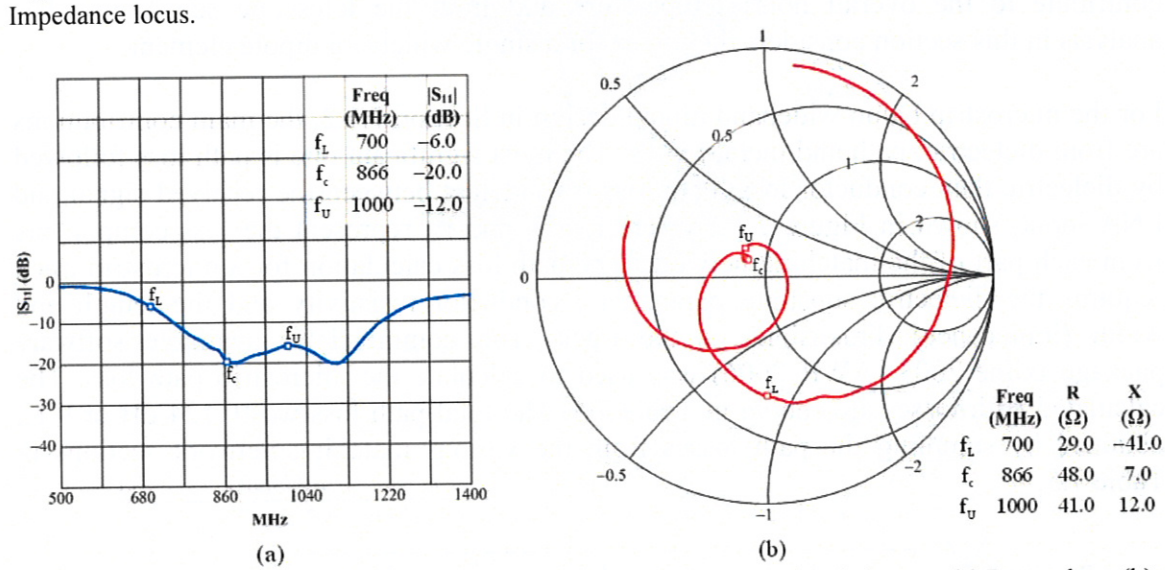

Figure 7.10 Measured horizontal polarisation performance for single isolated element. (a) Return loss. (b) Impedance locus.

Although the prototype feed did not meet the –10 dB return loss specification across the entire 700–1000 MHz band, the return loss was within this specification for frequencies up to around 1200 MHz. The frequency band over which a –10 dB return loss criterion is satisfied for both vertical and horizontal polarisations is shown in Table 7.4, where f_{BWL} and f_{BWU} are the lower and upper frequency bandwidth limits.

Polarisation	f_{BWL}	f_{BWU}	Bandwidth ratio
Vertical	763	1189	1.6:1
Horizontal	749	1206	1.6:1

Table 7.4 Measured impedance bandwidth for vertical and horizontal polarisations for –10 dB return loss.

The CST MWS model did not include the effect of the microstrip balun or baseboard network, but the shape of the simulated impedance locus, from 700–100 MHz, in Figure 7.7 is similar to the measured values. This similarity highlights an important characteristic in the design of the wideband feed because it is the shape of the impedance locus that indicates the broadband performance. If the impedance locus is more bunched and resembles a loop, then it has larger bandwidth compared to one that is a single curve

or has a 'tail', over the same frequency range. The job of the impedance matching network in this design is to transform the antenna impedance to the LNA impedance and the implementation of this network did not have a significant effect on the shape of the impedance locus. Therefore, the impedance simulation model could be used to optimise the wideband dipole geometry and reduce the 'tail' at 700 MHz and bunch the impedance locus to appear like a loop over the 700–1000 MHz range. Further optimisation of the design to improve the return loss at 700 MHz was not attempted here because the impedance performance will change in an array environment. Results for the impedance of a single element in an 8-element line feed are presented in Section 7.2.3.

7.1.3 Element Loss

Feed element losses, described in Section 2.7, are associated with the construction and choice of materials used in the design. Estimating these losses is important as they contribute to the overall noise temperature and limit the telescope sensitivity. The analysis in this section considers the losses for a single wideband dipole element.

For the microstrip balun wideband dipole design in Section 7.1.2, the main contributions are from dielectric, path and metal losses. The most significant one is path loss followed by dielectric then conductor loss. Path loss is modelled between the received signal and LNA input, shown in Figure 7.11, where L_1, L_2 and L_3 represent the loss components from each part of the matching network. The path loss calculation for a microstrip track requires the dielectric substrate parameters, conductor resistivity and the length and width (impedance) dimensions of the track. The commercially available software package txline 2003 (AWR 2006) was used to calculate the microstrip path loss. The calculated path losses are shown in Table 7.5. The total path loss was 0.124 dB or 9 K, obtained by summing the path losses from the various matching network sections in Table 7.5.

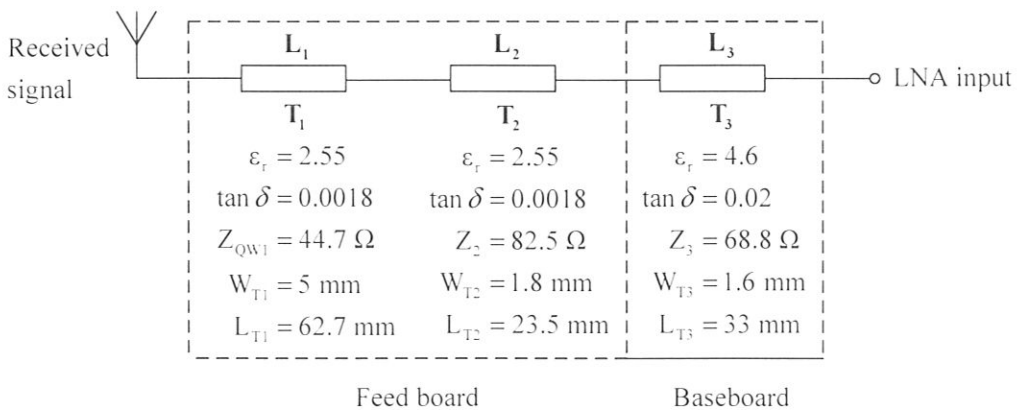

Figure 7.11 Path losses from the received signal to the LNA input.

Component	Path Length mm	Loss (dB/mm)	Path Loss (dB)
L1	62.7	0.00037	0.023
L2	23.5	0.0004	0.009
L3	33.0	0.0028	0.092

Table 7.5 Calculated path losses for the microstrip-fed wideband dipole design.

The path loss calculation includes contributions from the feed boards and baseboard, but losses on the arm board must also be considered. These losses were determined by using

a CST MWS model shown in Figure 7.12, by including a dielectric loss for the arm board and specifying an electrical conductivity instead of a PEC condition for the metal. In the simulations, the parameters used for the dielectric arm board FR4 substrate are shown in Table 7.1 and electrical conductivity was set to 5.8×10^7 S/m assuming a copper conductor. For the loss calculations, a post-processing function in CST MWS was used to obtain the results. This function calculated the dielectric and conductor losses as a ratio of peak loss divided by the total loss power. Calculated losses for the wideband dipole antenna arm board are given in Table 7.6, with the total loss being 0.058 dB or 4 K.

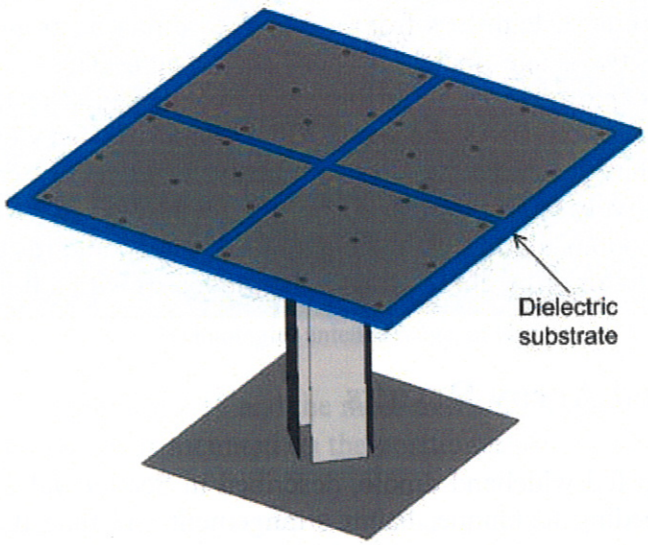

Figure 7.12 Simulation model for dielectric and conductor losses of wideband feed.

Losses	Simulated loss	$10\log_{10}(1-\text{loss})$ [dB]
Conductor	1.0×10^{-4}	0.0004
Dielectric	1.3×10^{-2}	0.058

Table 7.6 Simulated conductor and dielectric losses for arm board.

Estimating the overall loss for a single wideband feed element involves summing the path and arm board losses for a total of 0.18 dB or 13 K. Compared with the estimated 3 K loss for the present circularly polarised line feed element, in Table 2.2, the wideband element feed loss is relatively high. This is because the present line feed element is metallic in construction with no dielectric losses. In the new RF front-end architecture for SKAMP, the LNA is situated directly after the output of the in-pairs feeding point, so subsequent path and combining losses are minimised. Re-meshing the surface of the reflector is also planned, which will reduce the leakage temperature by around 15 K (D. Campbell-Wilson, personal communication, 2006).

Path losses for other feed options for the wideband dipole were estimated to compare with losses in the adopted two-stage quarter-wave matching network design. These other feed options were:

- Cable-fed balun plus a matching network.
- Single-stage quarter-wave matching network.
- Hybrid coupler feed.

A single-stage quarter-wave network is presented for comparison because it was unsuitable for the design, as discussed in Section 7.1.2. Calculations are presented in Appendix D and the total path losses for the various feed options are shown in Table 7.7.

Feed Network	Path Loss (dB)	Path Loss (K)
Adopted design	0.12	9
Single-stage*	0.09	6.3
Cable-fed	0.17	12
Hybrid coupler	0.84	64

Table 7.7 Estimated path loss for feed networks compared with the adopted two-stage matching network. *For comparison.

From Table 7.7, a hybrid coupler would result in an unacceptably high system temperature. In addition to the high noise temperature, the use of couplers substantially increases the design cost. Path loss from a cable-fed dipole is around 12 K, also higher than the adopted two-stage matching network design. This is because the fixed impedance of the cable requires a matching network placed after the balun rather than integrated with the balun, as is the case in the microstrip-fed design. A single-stage matching network has the lowest path loss but this was design was considered vulnerable because of the relatively large physical size of the feed tracks required for the microstrip board. Further reductions to the loss in the adopted design could result by selecting lower loss dielectric substrates or by eliminating dielectric losses with a fully metallised design.

7.2 Measured Array Results

A single microstrip-fed wideband dipole, described in Section 7.1.2, was constructed to test the in-pairs feeding technique, balun arrangement and tune the impedance match. This section presents measured pattern and impedance results for the dipole design in an 8-element line feed, shown in Figure 7.13. Mechanical dimensions of the ground plane are shown in Figure 6.7 and the dual channel dimensions are given in Section 6.4.2.

Element pattern measurements for the line feed prototype were conducted at the Argus Technologies antenna testing range at Kemps Creek, Sydney, Australia, over two days in October 2005. Figure 7.14 shows the ground reflection antenna test range with a bitumen surface area of approximately 306×40 m, and a Krupp elevation/azimuth positioner.

Figure 7.13 8-element wideband dual polarised dipole line feed prototype.

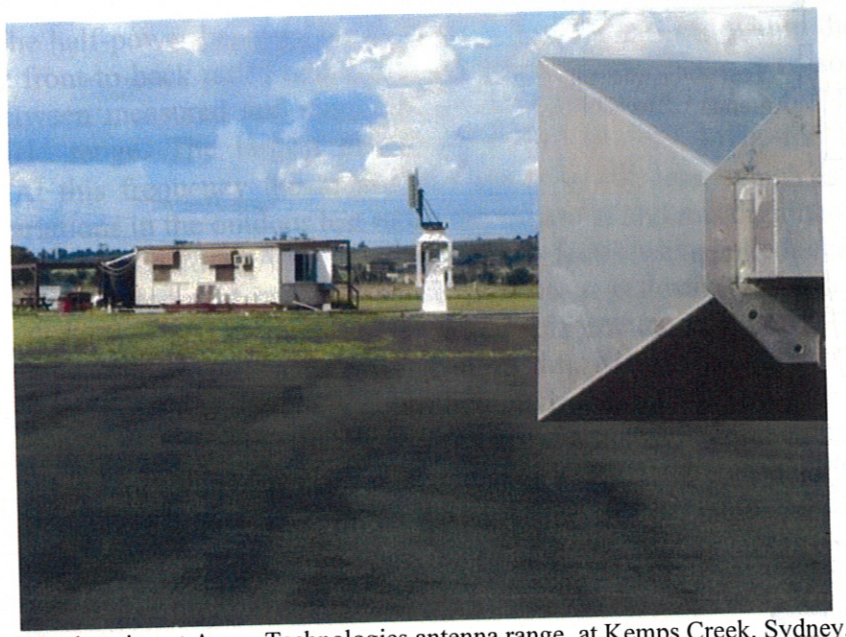

Figure 7.14 Feed testing at Argus Technologies antenna range, at Kemps Creek, Sydney, Australia.

The test setup is shown in Figure 7.15 and the measurement procedure follows:

- The antenna under test is mounted on the positioner using a windmill fixture. This is the receive antenna.
- A standard gain horn is the transmit antenna, placed at a distance, d = 100 m, from the receive antenna.
- The height of the standard gain horn, H_{tx} is set according to Equation 7.2 to ensure the direct ray and the ground reflected ray contribute in phase at the test antenna region.

$$H_{rx} = \frac{\lambda d}{4H_{tx}} \tag{7.2}$$

Where λ = free space wavelength

d = distance between transmit and receive antennas (100 m)

H_{rx} = receive antenna height

H_{tx} = transmit antenna height

- Measurements are made under computer control using Argus proprietary software, to calibrate the system and rotate the positioner to obtain radiation patterns.

Impedance measurements were made by placing the 8-element line feed in an anechoic chamber, to ensure a controlled environment with minimal reflections. The impedance of a single element in the array was measured to investigate mutual coupling in both polarisations compared to the results for a single element in isolation, shown in Figures 7.9 and 7.10. The measurement was made by connecting a single central element in the line feed to a network analyser, with matched 50 Ω impedances on the outputs of all the other elements in the array.

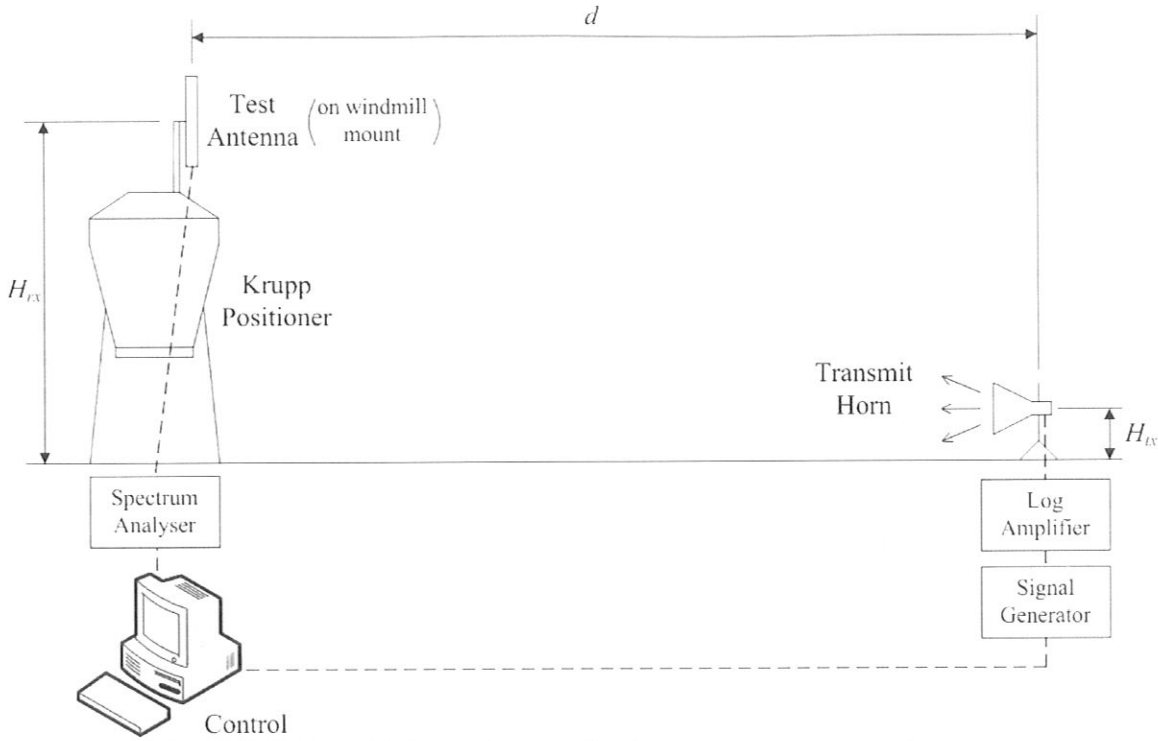

Figure 7.15 Argus Technologies ground reflection range antenna testing setup.

7.2.1 Transverse Plane Element Patterns

Element patterns in the transverse plane were measured by mounting the line feed vertically on the windmill with the feed aligned normal to the ground reflection range. Using the positioner, a full revolution in the azimuth direction was then used to obtain the radiation pattern. Element patterns at different scan angles were obtained by rotating the positioner to a selected elevation angle and then making a full revolution in the azimuth direction. Although the frequency range of the line feed was specified for 700–1000 MHz in Section 6.4.4, measurements were made up to 1100 MHz because the return loss remained around –10 dB. Patterns were not measured below 700 MHz because this was the lowest specified operating frequency of the standard gain horn used in the test setup. Scan angles greater 45° could not be measured at the test range because this was the elevation tilt limit for the positioner.

In summary, co- and cross-polar element patterns for vertical and horizontal polarisations were measured across a 700–1100 MHz range at 100 MHz intervals and at the centre frequency, 866 MHz, across a scan angle range of 0°–45° in 15° steps. These measurements were carried out once, but repeated if an anomalous reflection occurred in the pattern. From previous experience measuring antennas with half-power beamwidths > 80° at the test range, the average measurement error in beamwidth is around ±5°. This error occurs because antennas with broader beamwidths are more likely to pick up reflections from the outdoor range environment within their HPBW range. Therefore, a smoothing function is applied to the element patterns to reduce the impact of range reflections. This improves the beamwidth error to ±3° and pattern measurement error to around ±3 dB. The beamwidth measurement error reduces for antennas with narrower beamwidths because fewer reflections are captured within their HPBW range.

Table 7.8 contains measured element pattern parameters for the line feed prototype at 0° scan angle. The half-power beamwidths for both polarisations were within the 70°–100° range and the front-to-back ratios met the 25 dB specification. There is reasonably good agreement between measured and simulated beamwidths (from Table 6.3[1]) across the 700–1000 MHz range. The largest difference occurs at 900 MHz for the vertical polarisation. At this frequency the measured HPBW is 10° less, which is due to the unexpected variations in the outdoor test range environment and misalignment of the arm board in the array construction. Although a smoothing factor was applied, certain objects in the test range environment can still cause significant reflections depending on the measurement frequency and azimuth angle. When this occurs, the pattern has a slight modulation, which can produce a narrower beamwidth. Measurements in the anechoic chamber and the simulations assume a controlled environment with no such reflections. A better comparison to determine the difference between measured and simulated results is to use the edge taper value at the subtended half angle, ±88°, as it is unlikely that reflections will occur at both ±88° azimuth limits. Using this parameter, the largest edge taper difference between measured and simulated results is within the pattern measurement error.

Freq (MHz)	Vertical Polarisation				Horizontal Polarisation			
	HPBW (°)	Edge taper (dB)	F/B (dB)	XPR (dB)	HPBW (°)	Edge taper (dB)	F/B (dB)	XPR (dB)
700	88	–12	27	–16	80	–15	28	–13
800	80	–13	26	–13	86	–15	28	–19
866	82	–15	25	–16	81	–15	29	–18
900	76	–15	26	–15	84	–15	33	–17
1000	81	–15	32	–17	78	–15	28	–18
1100	77	–15	33	–21	80	–15	34	–16

Table 7.8 Measured dual channel feed parameters for vertical and horizontal polarisations at 0° scan angle.

Measured beamwidth variation across the frequency range for different scan angles is plotted in Figure 7.16. These results show that the beamwidths for both the vertical and horizontal polarisations remain within the 70°–100° limits across the frequency and scan angle ranges. The front-to-back ratios across the frequency range generally decrease with increasing scan angle, for both polarisations, as shown in Figure 7.17. The decrease in F/B at 45° for the measured result is less than the equivalent simulated result (from Figure 6.18) over a 700–1000 MHz frequency range. The minimum F/B at 45° scan angle for the vertical polarisation was 20 dB for the measurement and 18 dB for the simulated result, whereas for the horizontal polarisation the minimum F/B was 23 dB for the measurement and 18 dB for the simulation. Edge tapers for vertical and horizontal polarisations, shown in Figure 7.18, are matched within 5 dB on both polarisations for a 800–1100 MHz frequency range across the 0°–45° scan angle range. There is a larger edge taper difference below 800 MHz at 45° scan angle, caused by the pattern narrowing on the horizontal polarisation. There is good agreement between measured and simulated edge tapers (in Figure 6.19) with a maximum of 3 dB difference between all results except for 700 MHz at 45° scan angle on the horizontal polarisation, where the difference is 5 dB.

[1]Simulations cover a slightly different frequency range (500–1000 MHz) compared with measurements.

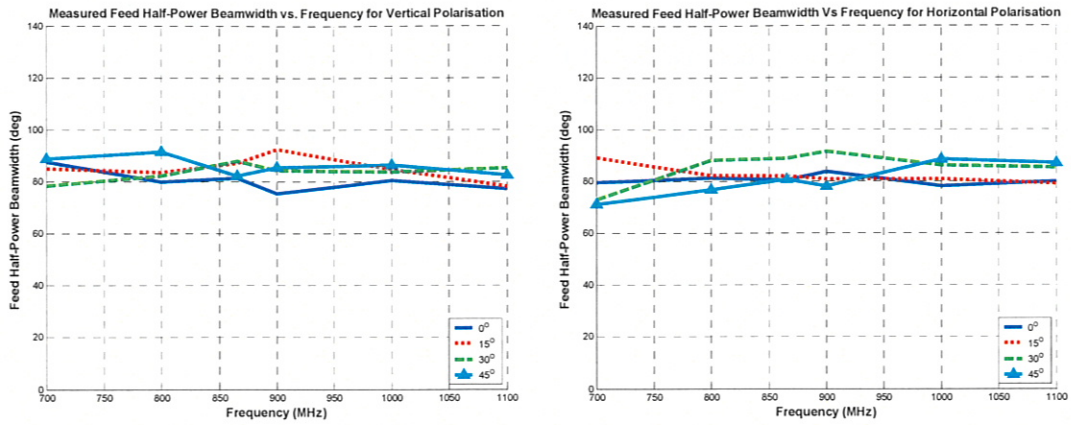

(a) (b)

Figure 7.16 Measured half-power beamwidth across 700–1100 MHz, over 0°–45° scan angle. (a) Vertical polarisation. (b) Horizontal polarisation.

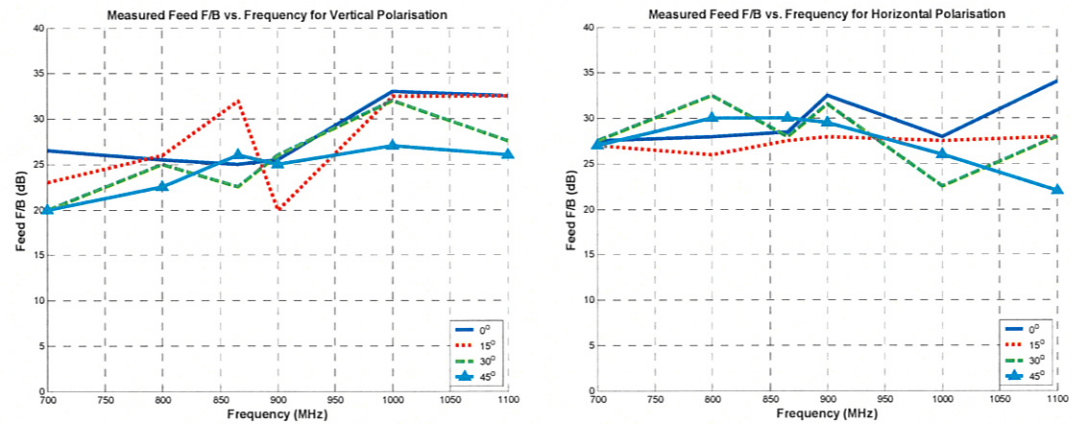

(a) (b)

Figure 7.17 Measured front-to-back ratio across 700–1100 MHz, over 0°–45° scan angle. (a) Vertical polarisation. (b) Horizontal polarisation.

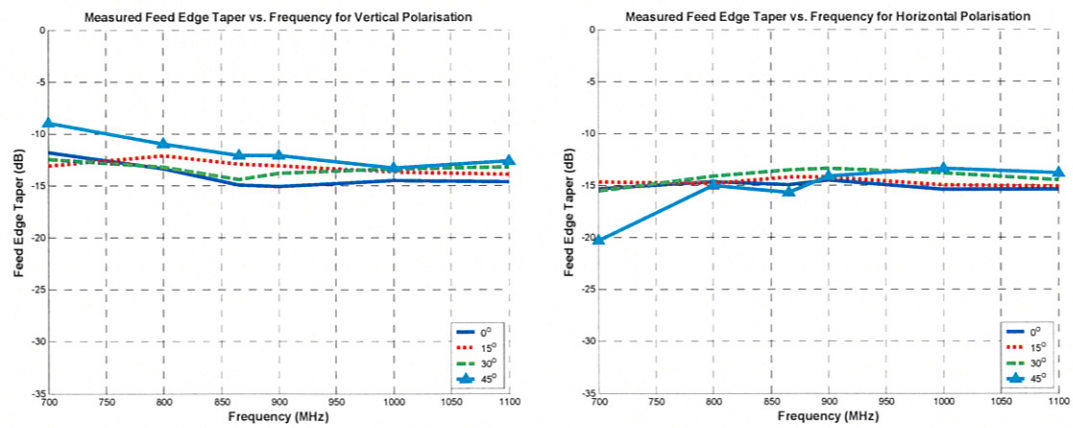

(a) (b)

Figure 7.18 Measured edge taper across 700–1100 MHz, over 0°–45° scan angle. (a) Vertical polarisation. (b) Horizontal polarisation.

The beamwidth difference between the orthogonal polarisations in Figure 7.19 shows that the beamwidths are matched within ±18° across the 700–1100 MHz frequency range for the 0°–45° scan angle range. Comparing the measured beamwidth difference with the

simulated beamwidth difference (from Figure 6.20) shows that the simulated beamwidths are matched within ±12° for scan angles up to 45°. Measured cross-polar ratios at 0° scan angle for both polarisations are shown in Figure 7.20. The XPR within the subtended half-angle range, ±88°, is less than –15 dB for both vertical and horizontal polarisations. Ideally there should be no cross-polar component at 0° azimuth angle and the cross-polar ratio should be symmetric about 0° azimuth angle as shown for the simulated results from Figure 6.16. However, there are contributions in the measured result from cross-polar currents generated by the microstrip balun, element construction and the polarisation characteristics of the ground reflection test range.

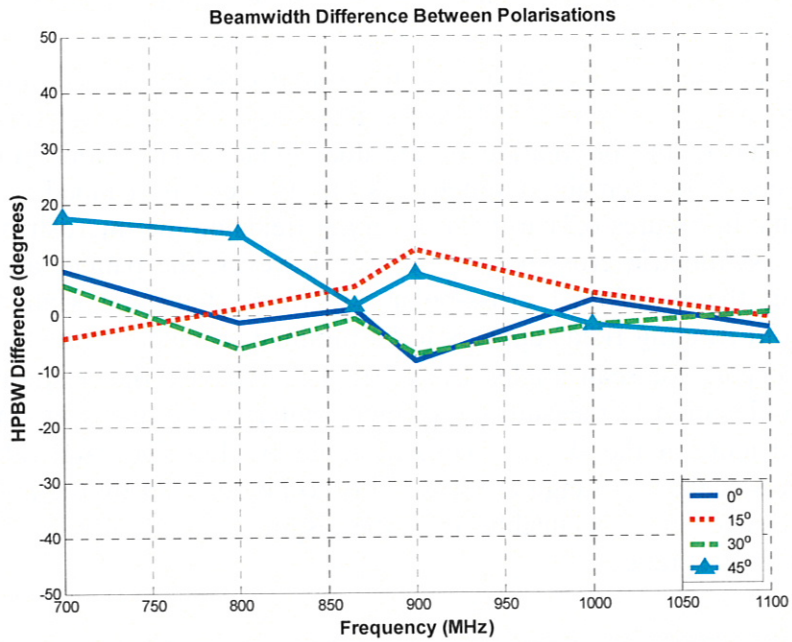

Figure 7.19 Measured half-power beamwidth difference between orthogonal polarisations across 700–1100 MHz band, over 0°–45° scan angle.

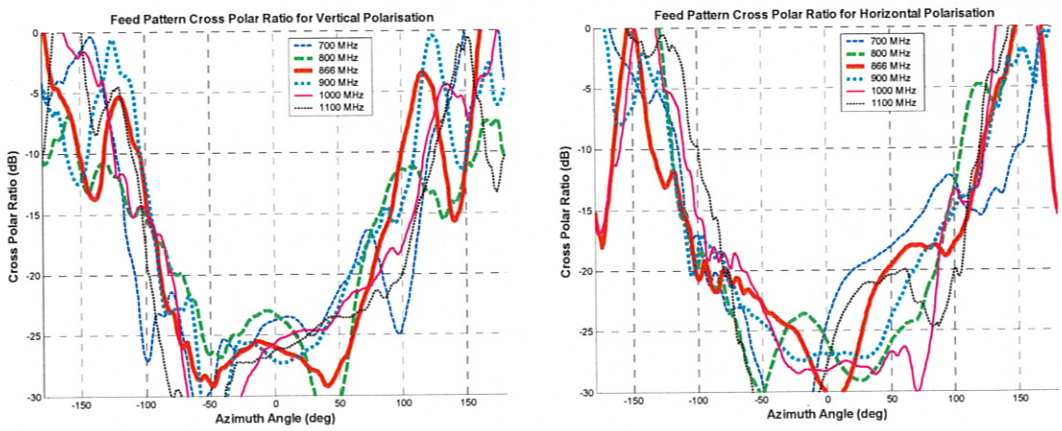

(a) (b)

Figure 7.20 Measured cross-polar ratio for the dual channel line feed at 0° scan angle across 700–1100 MHz band. (a) Vertical polarisation. (b) Horizontal polarisation.

Measured transverse element patterns for vertical and horizontal polarisations across the frequency and scan range are shown in Figures 7.21 to 7.24. Cross-polar levels on both polarisations increase as the scan angle is increased. The broadening of the co-polar

pattern and increase in back radiation levels is more pronounced for the vertical polarisation than it is for the horizontal polarisation. This effect was also shown in the simulated results for the vertical polarisation in Figures 6.21(a) to 6.24(a) and is caused by the alignment of the vertical polarisation in the scanning direction, as explained in Section 6.4.3. In all of the pattern measurements there is a slight gain modulation at azimuth angles ranging from –150° to –50°. This is due to scattering effects at the test range from the corrugated iron shed and control hut, shown in Figure 7.14. Although a smoothing factor has been applied to the patterns to reduce this effect, the modulation is still apparent.

The unexpected cross-polar radiation at 0° scan angle in Figure 7.21 was explained previously. Cross-polar levels at 0° scan angle in Figure 7.21 are < –23 dB for the vertical polarisation and < –21 dB for the horizontal polarisation. Although the cross-polar levels did not go to zero for 0° scan angle, they should be symmetric about 0° azimuth angle due to the orientation of the dual linear polarisation. Furthermore the cross-polar levels should remain symmetric as the line feed is scanned as shown in the simulated results, in Figures 6.21 to 6.24. Fringing fields on the microstrip balun boards could produce asymmetric cross-polar patterns. However, the pattern asymmetries are not mirrored in the orthogonal cross-polar pattern at the same scan angle, so the contribution from fringing fields appears to be minimal. Greater symmetry in the cross-polar patterns occurs for scan angles from 30°–45°. Because the positioner was tilted back further in elevation to measure the element patterns at larger scan angles, the line feed is directed more at the sky for azimuth angles within ±90° and reflections from scattering objects at the test range are less likely to be detected by the antenna at large scan angles. Hence, it is plausible that the asymmetry is due to the scattering environment at the test range.

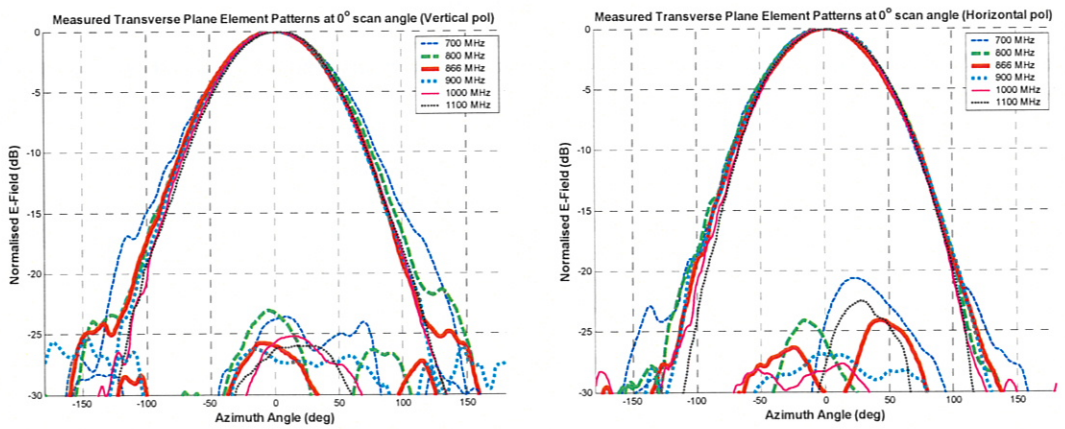

(a) (b)

Figure 7.21 Measured co- and cross-polar patterns at 0° scan angle across 700–1100 MHz band. (a) Vertical polarisation. (b) Horizontal polarisation.

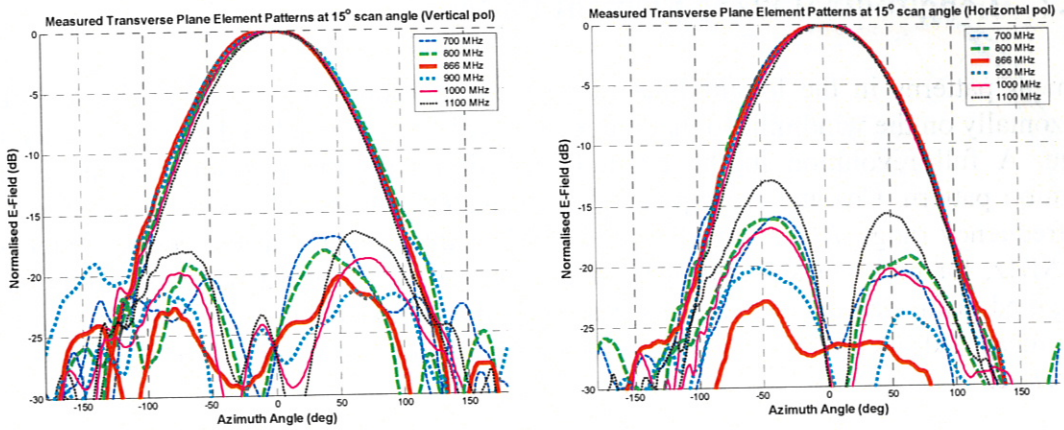

(a) (b)

Figure 7.22 Measured co- and cross-polar patterns at 15° scan angle across 700–1100 MHz band. (a) Vertical polarisation. (b) Horizontal polarisation.

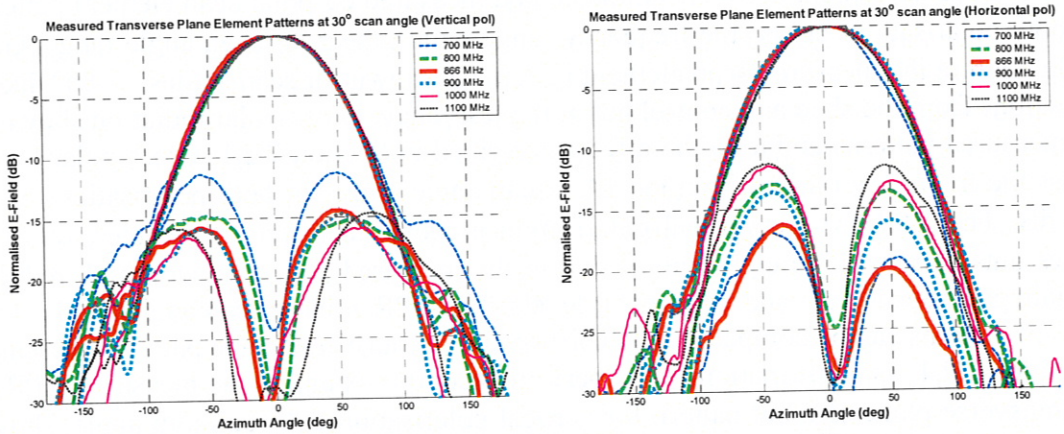

(a) (b)

Figure 7.23 Measured co- and cross-polar patterns at 30° scan angle across 700–1100 MHz band. (a) Vertical polarisation. (b) Horizontal polarisation.

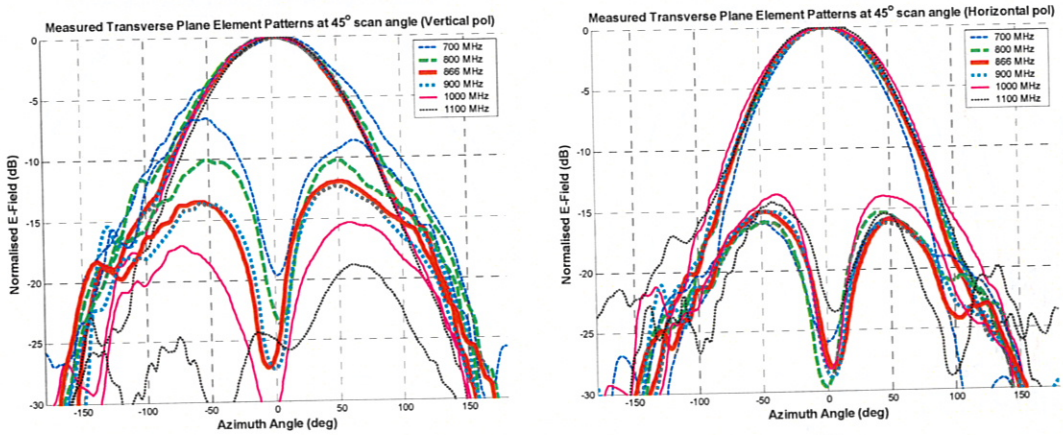

(a) (b)

Figure 7.24 Measured co- and cross-polar patterns at 45° scan angle across 700–1100 MHz band. (a) Vertical polarisation. (b) Horizontal polarisation.

7.2.2 Longitudinal Plane Element Patterns

Element patterns in the longitudinal plane were measured by mounting the line feed horizontally on the windmill, so that the feed was aligned parallel to the ground reflection range. A full revolution in the azimuth direction with the positioner produced the radiation pattern. Co- and cross-polar element patterns in this plane were measured for the frequency range 700–1100 MHz in 100 MHz intervals and at the centre frequency, 866 MHz, for both vertical and horizontal polarisations. Element patterns in this plane are called scan element patterns, as described in Section 6.4.4. Scan element patterns were measured once and a smoothing factor was applied to reduce reflections from the test range.

Simulated scan element patterns are shown in Figure 7.25 across the frequency range 700–1100 MHz for comparison with the measured results in Figure 7.26. Cross-polar levels in the simulated results are < –30 dB on both polarisations and are not shown. There is good agreement between simulated and measured co-polar scan element patterns for both polarisations across the frequency range within the ±45° scan angle range. Gain modulation in the measured scan element patterns is shown for scan angles < –50° due to reflections from the shed and control hut at the test range. Cross-polar radiation shown in the measured patterns is due to the effects described in Section 7.2.1. Cross-polar levels across the frequency range within the ±45° scan angle range for both polarisations are < –22 dB. The XPR for the vertical polarisation is worse at lower frequencies, for scan angles outside the ±45° range. This is due to the increased pattern taper which reduces the gain gap between co- and cross-polar levels. The XPR at large scan angles in the scan element patterns can be compared with corresponding transverse plane patterns presented in Section 7.2.1, as confirmation of the performance. For example, the measured XPR in the transverse plane element pattern for vertical polarisation at 0° azimuth angle, shown in Figure 7.24(a), for 700 MHz at 45° scan angle is around –19 dB and the corresponding XPR at 45° scan angle in Figure 7.26(a) is around –18 dB.

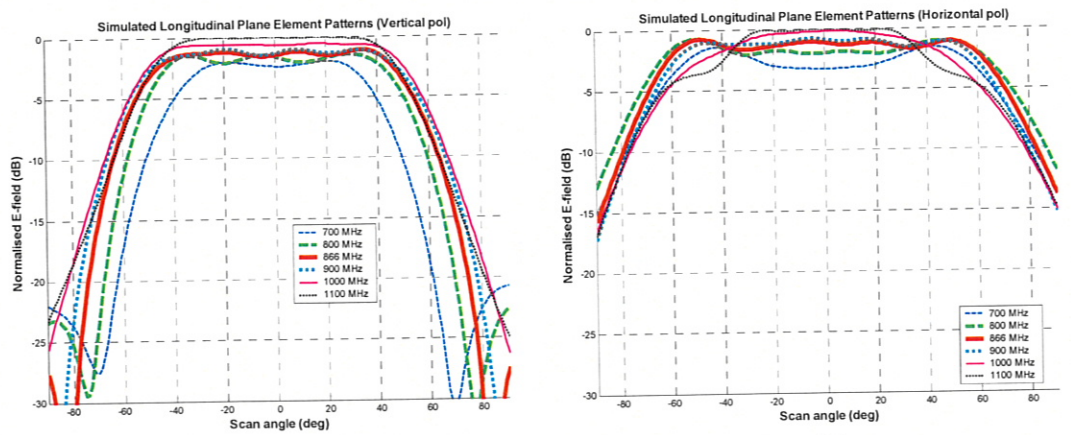

(a) (b)

Figure 7.25 Simulated scan element patterns across a 700–1100 MHz band. (a) Vertical polarisation. (b) Horizontal polarisation. *Note: cross-polar levels are < –30 dB on both polarisations.

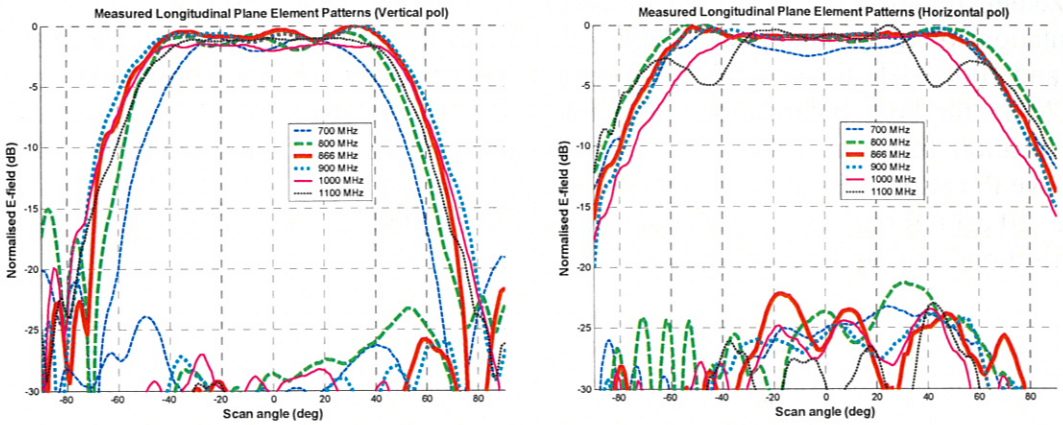

(a) (b)

Figure 7.26 Measured scan element patterns across a 700–1100 MHz band. (a) Vertical polarisation. (b) Horizontal polarisation.

There is a slight asymmetry shown in the measured co-polar scan element patterns because there is no single central element in an array with an even number of elements. Gain ripples within the flat part of the scan element pattern are more prominent in the measured results compared to the simulated results. Reasons for this include reflections from the outdoor measurement environment and coupling from the microstrip balun. In the measured horizontal polarisation, in Figure 7.26(b), there is a 5 dB null at 1100 MHz for ±45° scan angle. This null is shown in the simulated scan element pattern, but it is about 2 dB smaller than the measured result. Because the null occurs at both ±45° scan angles, this is primarily a line feed effect and indicates a possible resonance in the transverse element pattern. To check the likelihood of this reason, the horizontal polarisation element pattern for 1100 MHz at 45° scan angle is studied (Figure 7.24(b)). The back radiation increases at azimuth angles from –180° to –100° whereas the cross-polar levels remain around –15 dB. The increase in back radiation occurs at the azimuth region where the hut and shed are located and hence, it is uncertain whether the increase is due only to the line feed. Another limitation caused by operating at large scan angles at 1100 MHz is the appearance of grating lobes in the field-of-view, which is investigated in Section 7.4.

7.2.3 Impedance

The impedance of a single element in the 8-element line feed, shown in Figure 7.13, was measured to investigate the effects of mutual coupling and to compare with the results measured for a single element in isolation, presented in Section 7.1.2. The measurement was performed in an anechoic chamber and consisted of feeding a central element in the line feed and terminating all the other elements in the array using 50 Ω loads. Elements either side of the central element were also measured, which produced similar results.

Measured return loss and impedances for the vertical and horizontal polarisation are shown in Figures 7.27 and 7.28. The impedance measurement was referenced to the in-pairs combining point, which is the LNA input. Impedance loci measurements for a single element in an array differ from the loci for a single element in isolation (Figures 7.9(b) and 7.10(b)), because of coupling from surrounding elements. Furthermore, the impedances for the vertical polarisation in Figure 7.27(b) are different from the

horizontal polarisation in Figure 7.28(b) because of their respective polarisation orientations on the ground plane. Table 7.9 contains the return loss and impedance at 700, 866 and 1000 MHz for vertical and horizontal polarisations. The measured return loss at 700 MHz for both polarisations does not quite achieve the –10 dB line feed design specification listed in Table 6.1. An impedance simulation model could be used to improve the return loss at the lower frequency, as part of future research. The bandwidth for a –10 dB return loss on both polarisations is presented in Table 7.10, with the vertical polarisation limiting the bandwidth to 1.5:1.

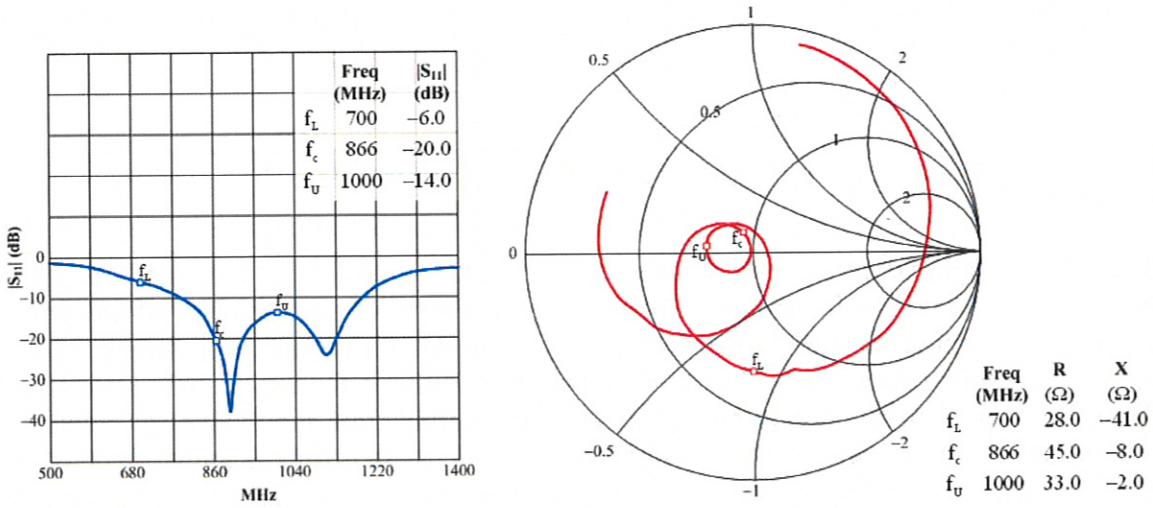

(a) (b)

Figure 7.27 Measured vertical polarisation for one element in an 8-element module (a) Return loss. (b) Impedance.

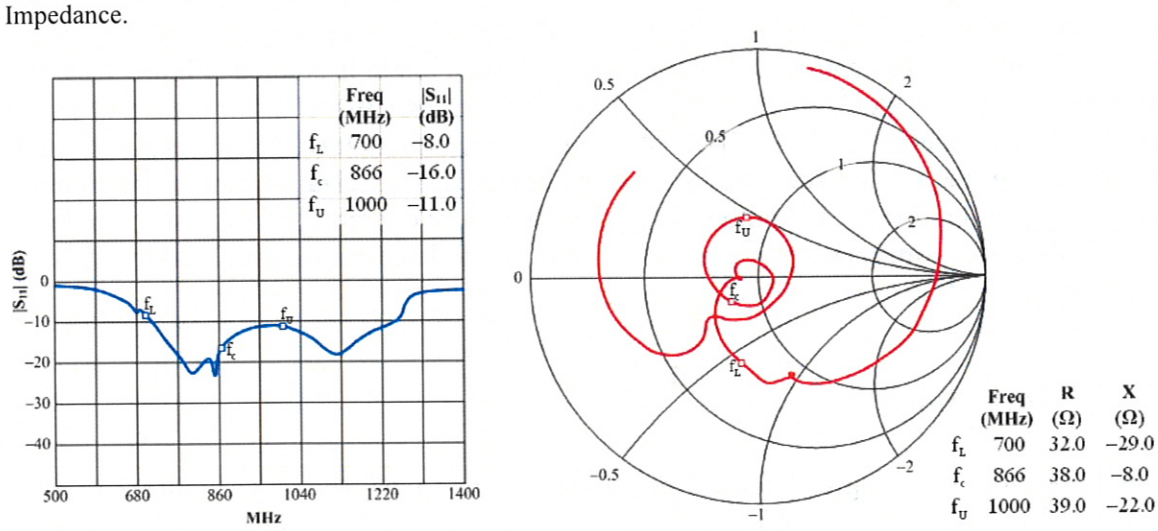

(a) (b)

Figure 7.28 Measured horizontal polarisation for one element in an 8-element module (a) Return loss. (b) Impedance.

Frequency (MHz)	Return Loss (dB)		Impedance (Ω)	
	Vertical pol	Horizontal pol	Vertical pol	Horizontal pol
700	–6	–8	28 – j41	32 – j29
866	–20	–16	45 – j8	38 – j8
1000	–14	–11	33 – j2	39 – j22

Table 7.9 Measured return loss and impedance for a single element in an 8-element module.

Polarisation	f_{BWL}	f_{BWU}	Bandwidth ratio
Vertical	789	1186	1.5:1
Horizontal	714	1254	1.8:1

Table 7.10 Measured impedance bandwidth for a single element in an 8-element module for vertical and horizontal polarisations for a –10 dB return loss.

The return loss plot for the vertical polarisation showed a smooth variation with no uncharacteristic resonances, whereas a resonance occurred for the horizontal polarisation at 850 MHz. This resonance could indicate a blind angle or incorrect element implementation. The measured impedance for a single element in isolation for horizontal polarisation, shown in Figure 7.10, did not show this resonance. Hence, the resonance is unlikely to be due to the element design. Although not presented, an equivalent impedance measurement was undertaken for a 4-element cable-fed line feed to verify the element patterns in Section 7.1.1. The cable-fed line feed also showed a single resonance appearing at the horizontal polarisation around 850 MHz, eliminating the microstrip or cable feed as the primary cause of this resonance. The resonance was still present in the impedance when the channels were removed, as confirmed by a simulation using CST MWS. By a process of elimination, the primary cause of this resonance is probably the array configuration and mutual coupling from surrounding elements. The resonance occurs because the horizontal polarised mutual coupling currents are affected by the finite edge of the plane, particularly at large scan angles. Resonances due to mutual coupling are also likely to occur for the vertical polarisation as the line feed is scanned, because this polarisation is orientated in the direction of the scanning plane. Simulated scan impedance results, in Section 6.4.6, indicate cases where the scan resistance goes to zero for particular scan angles. However, the experimental measurement of the scan impedance is difficult and requires specialist hardware, as described in Section 6.1.1, and was not undertaken in the current work.

With the inevitable appearance of resonances due to mutual coupling, causing pattern degradation and blind angles, the question arises: how will the telescope performance be affected? Instrumental effects which are repeatable and characterisable can be calibrated. Therefore, resonances in the input impedance due to the array geometry can be corrected, but imaging at the affected bandwidth is not possible. The new spectral line correlator for SKAMP, along with polyphase filter banks, will produce 6000 spectral channels across the 100 MHz instantaneous bandwidth. Selective deletion will avoid image or spectral distortion.

7.3 Aperture Efficiency

The aperture efficiency, η_{ap}, for a reflector antenna is multiplied by the physical collecting area to obtain the effective area, A_{eff}. The aperture efficiency has an inverse relationship with the system sensitivity, in Equation 2.22. Calculating the aperture efficiency involves the multiplication of several sub-efficiencies in Equation 3.2, being those from the taper, η_t, spillover, η_{sp}, blockage, η_{blk}, and polarisation, η_{pol}. The sub-efficiencies and aperture efficiency for the wideband line feed, in the transverse plane require the measured transverse element patterns from Section 7.2.1 and were calculated using Equations 3.2, 3.4, 3.5, 3.7 and 3.8 for η_{ap}, η_t, η_{sp}, η_{blk} and η_{pol}, across the frequency and scan angle range. Results for the measured sub-efficiencies and aperture efficiency across the scan angle range at the centre frequency, 866 MHz for the vertical

and horizontal polarisations are shown in Figure 7.29. Measured sub-efficiencies and aperture efficiency at other frequencies across the 700–1100 MHz range are presented in Appendix E, Figures E.1 to E5.

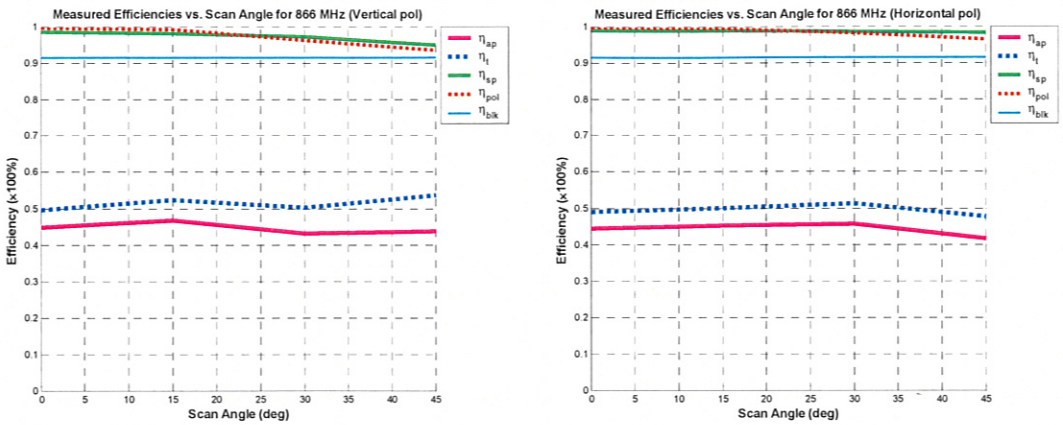

(a) (b)

Figure 7.29 Measured efficiency at 866 MHz. (a) Vertical polarisation. (b) Horizontal polarisation.

The taper efficiency range is around 0.45–0.6 for both polarisations across the frequency and scan angle range. Figures E.1(a) to E.5(a) show that the vertical polarisation taper efficiency generally increases with scan angle. This is reflected in the corresponding transverse element patterns at 45° scan angle in Figure 7.24(a), which shows an increase in edge taper and back radiation levels. The spillover efficiencies for vertical and horizontal polarisations are > 0.92 across the frequency and scan angle range. Polarisation efficiencies for vertical and horizontal polarisations are > 0.92 across the frequency and scan angle range except at 700 MHz for the vertical polarisation at 45° scan angle, where the increased cross-polar levels give a 0.84 efficiency. From this analysis it is shown that the limiting sub-efficiency is the taper efficiency. This is caused by the relatively deep reflector geometry (f/D = 0.26), which is difficult to illuminate efficiently without increasing the amount of spillover.

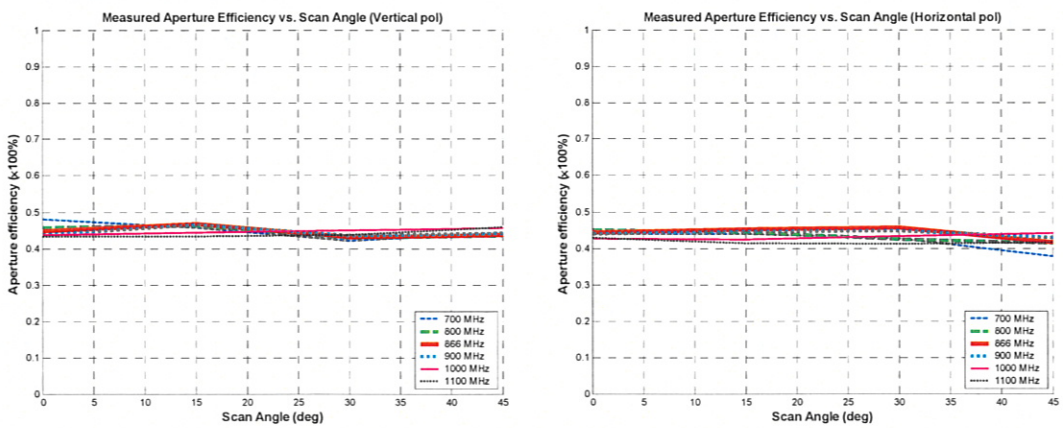

(a) (b)

Figure 7.30 Measured aperture efficiency for 0°–45° scan angle and 700–1100 MHz frequency. (a) Vertical polarisation. (b) Horizontal polarisation.

Aperture efficiencies for vertical and horizontal polarisation for the 700–1100 MHz band and 0°–45° scan angle range are shown in Figures 7.30(a) and 7.30(b). The aperture

efficiency across the operating range for the vertical polarisation was 0.42–0.48 and for the horizontal polarisation 0.38–0.46. The worst aperture efficiency for the horizontal polarisation occurred at 700 MHz for a 45° scan angle. This is confirmed from Figure 7.18(b), where the edge taper value reduces to –20 dB and Figure 7.24(b) shows the narrowing of the radiation pattern.

The design goal for the line feed aperture efficiency was specified in Section 3.3.1 as 0.5, which is current MOST narrowband feed aperture efficiency. The wideband line feed failed to meet this design goal for both polarisations by a few percent. Achieving this specification was difficult due to the wideband, dual-polarisation and scanning requirements for the new feed. The primary limitation in achieving the 0.5 aperture efficiency is the retention of the existing reflector. In reflector antenna design, the feed and reflector are usually optimised together to achieve an average aperture efficiency around 0.65 (Stutzman and Thiele 1998). A suitable reflector geometry for the wideband line feed has an $f/D = 0.31$, which would provide an aperture efficiency > 0.5, for both polarisations as shown in Figure 7.31.

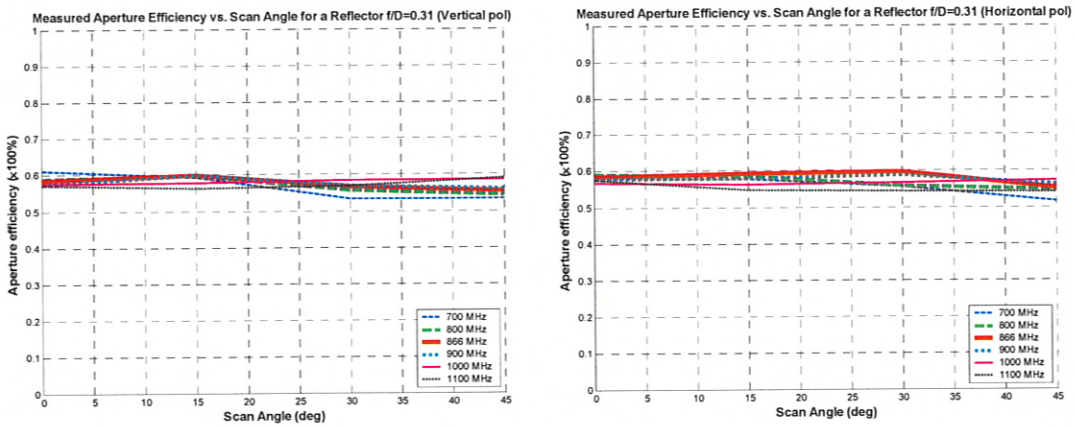

(a) (b)

Figure 7.31 Measured η_{ap} for a reflector geometry with a $f/D = 0.31$, across the 0°–45° scan angle and 700–1100 MHz frequency. (a) Vertical polarisation. (b) Horizontal polarisation.

7.4 Grating Lobe Analysis

The analysis in this section considers the loss in signal due to grating lobes, which are dependent on the array geometry and element spacing of the line feed. These grating lobes are different from the lobes produced by the periodic combining of contiguous line feed sections which are called quantisation lobes, as described in Section 2.6.

Grating lobes appear in the field-of-view for a line feed at large scan angles and element spacings, with the angle of the lobe determined by Equation 3.11. Once the grating lobe angle is determined, the measured scan element pattern in Figure 7.26 can be used to obtain its magnitude. This technique is also used to obtain the magnitude of the main beam at the desired scan angle. In the line feed design an acceptable scan angle range was specified as ±45°, limited by pattern degradation and gain reduction outside this range, as described in Section 6.4.3 and 6.4.4. For the new line feed design with a

maximum scan angle, θ_{max}, a grating lobe will appear in the observing region at the frequency, λ, for the fixed element spacing, $d = 173$ mm, determined by (Hansen 1966b):

$$d = \frac{\lambda}{1 + \sin\theta_{max}} \tag{7.3}$$

Where the observing region refers the angular region within the maximum scan angle limits: $\pm\theta_{max}$.

Using Equation 7.3, a grating lobe appears for a maximum scan angle of 45° from about 1000 MHz. Although the scan angle range was defined as ±45° for acceptable line feed performance, it is likely that the telescope will operate out to ±60° to obtain better Hour Angle (HA) coverage for astronomical observations. Therefore, the grating lobe loss will be analysed up to this scan angle range. A comparison of the grating lobe magnitude and main beam magnitude for vertical and horizontal polarisations at 1000 MHz and 1100 MHz are shown in Figures 7.32 and 7.33.

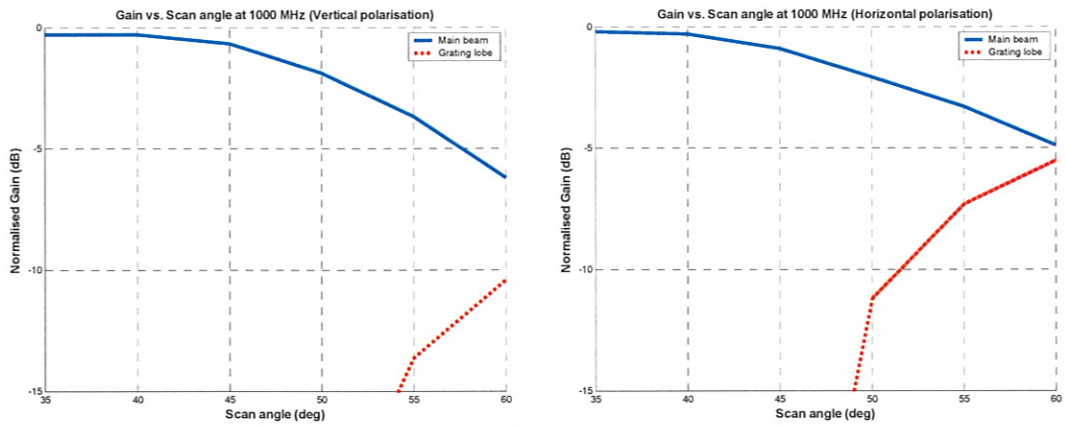

(a) (b)

Figure 7.32 Comparison of main beam and grating lobe at scan angles 35°–60° for 1000 MHz. (a) Vertical polarisation. (b) Horizontal polarisation.

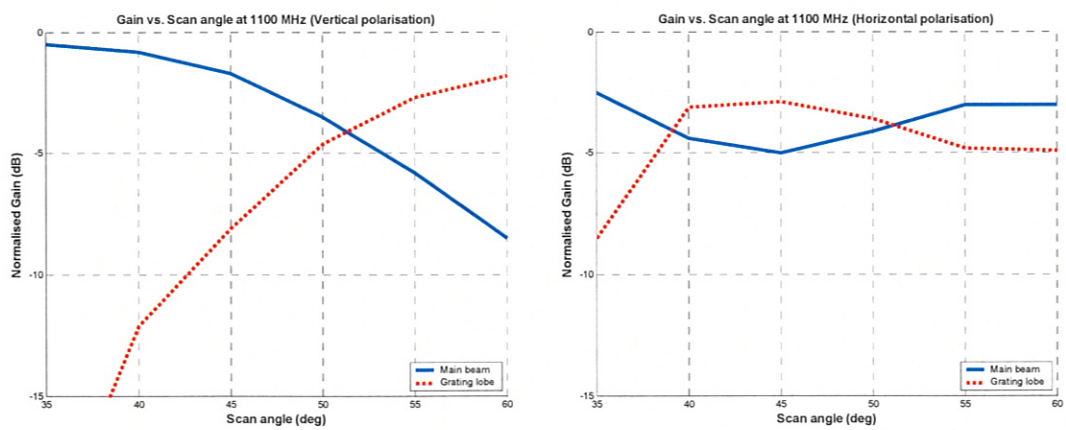

(a) (b)

Figure 7.33 Comparison of main beam and grating lobe at scan angles 35°–60° for 1100 MHz. (a) Vertical polarisation. (b) Horizontal polarisation.

The difference in grating lobe magnitude for vertical and horizontal polarisations is due to their respective polarisation orientations, which results in different scan element

patterns (Figure 7.26). A large taper in the scan element pattern for the vertical polarisation causes a reduced grating lobe magnitude compared to the horizontal polarisation. At a frequency of 1000 MHz for the vertical polarisation in Figure 7.32(a), the grating lobe magnitude is –10 dB down from the main beam at a scan angle of 55°. For the horizontal polarisation, in Figure 7.32(b), the grating lobe magnitude is –10 dB from the main beam at around 50° scan angle. At 60° scan angle, the difference in magnitude between the main beam and grating lobe for the horizontal polarisation is around 0.6 dB and for the vertical polarisation it is around 4 dB. At a frequency of 1100 MHz for the vertical polarisation, in Figure 7.33(a), the grating lobe magnitude is –10 dB from the main beam at a scan angle around 42°. The grating lobe magnitude becomes greater than the main beam magnitude for scan angles > 51°. For the horizontal polarisation the grating lobe magnitude is around –6 dB from the main beam at 35° scan angle. There is a null in the main beam magnitude around 45° scan angle, which indicates a degradation in radiation performance around this angle. This null also causes the grating lobe magnitude to become greater and then less than the main beam across the 35°–60° scan angle range. This result suggests that the grating lobe is the likely cause of the null at ±45°, as discussed in Section 7.2.2. More power is radiated from the grating lobe than the main lobe, causing a drop in the magnitude of the main beam. Results for the grating lobe magnitude < 35° are not shown for 1100 MHz because 35° is θ_{max} or the angle at which the grating lobe comes into the field-of-view at this frequency, calculated using Equation 7.3. Thus the grating lobe limits the radiation performance for the horizontal polarisation at 1100 MHz to scan angles within ±35°.

7.5 Summary

Experimental implementation of the in-pairs feeding technique for the wideband dual polarised feed element and evaluation of the measured array performance were presented. A feed prototype using cable baluns was measured to investigate element patterns. These patterns showed good agreement with simulated results, thus validating the correct in-pairs excitation method. However, due to problems in construction and alignment in the cable-fed design, an alternative microstrip balun was designed. This design enabled the integration of an impedance matching network with the balun, which reduces element path loss. The –10 dB return loss bandwidth for a single element was 1.6:1, which spanned a frequency range of around 750–1200 MHz on both polarisations. The expected element loss for the microstrip fed wideband dipole feed is calculated to be around 13 K and it was shown that the path loss was the limiting feed noise parameter.

Measurements of an 8-element microstrip-fed wideband dipole were presented in Section 7.2, to investigate the effects of the balun and mutual coupling on the radiation and impedance performance. Transverse plane element patterns for vertical and horizontal polarisation, across a 700–1100 MHz frequency range and 0°–45° scan angle range showed good agreement with the simulated results presented in Section 6.4.2 and 6.4.3. Measured results showed similar degradation in radiation performance with increasing scan angles and increased degradation on the vertical polarisation at the lower frequency range and large scan angles. Cross-polar radiation appeared at 0° scan angle due to element misalignment and test range characteristics. The scattering environment at the range caused asymmetric cross-polar patterns which were more prevalent at lower scan angles. Scan element patterns measured in the longitudinal plane were presented in

Section 7.2.2. Again there was good agreement with simulated patterns, with the measured patterns exhibiting similar characteristics such as increased pattern tapering on the vertical polarisation and gain modulation in the scan angle region due to mutual coupling. Cross-polar radiation appears in the measurements due to the same reasons described for the transverse plane element patterns. The cross-polar levels for both polarisations are less than –22 dB below the peak across the 700–1100 MHz frequency range and 0°–45° scanning range. The impedance of a single element was measured in an 8-element array to investigate the effect of mutual coupling. The return loss and impedance are different for vertical and horizontal polarisations, due to the difference in mutual coupling environment between polarisations. The limiting impedance bandwidth for a –10 dB return loss was 1.5:1, from the vertical polarisation. A resonance occurred in the impedance measurement for the horizontal polarisation around 850 MHz, due to the array configuration and mutual coupling from surrounding elements.

An aperture efficiency analysis was conducted to investigate the wideband line feed performance in the MOST reflector. This analysis showed the average aperture efficiency was 0.45 for the vertical polarisation and 0.42 for the horizontal polarisation over a 700–1100 MHz frequency range and 0°–45° scan angle range. The limiting sub-efficiency was the taper efficiency, due to the difficulty in illuminating the deep reflector of the MOST ($f/D = 0.26$). The wideband line feed did not meet the 0.5 design goal for the aperture efficiency. Although the feed beamwidth could be increased to improve the taper efficiency, this would cause an increase in spillover temperature. A grating lobe analysis investigated the magnitude of the grating lobe compared to the main beam at the upper operating frequency limit. At a frequency of 1100 MHz, grating lobes limit the scan angle range of the vertical polarisation to ±35°.

Chapter 8

Wideband Feed Reflector Patterns

This Chapter describes a methodology for simulating reflector patterns using the measured feed patterns presented in Chapter 7. Simulating the reflector pattern provides performance parameters, which are not determined from just the feed measurements and include the reflector sidelobe levels, half-power beamwidth, cross-polar ratio in the main beam and reflector temperature. The measured feed patterns in the cylindrical reflector environment are presented in Section 8.1. These simulations use the same programs described in Chapter 5. Results are presented in Section 8.2 and an estimate of the noise temperature from the line feed is provided by calculating the spillover temperature from the measured feed patterns. A reflector pattern simulation using an asymmetric feed pattern is described in Section 8.3, to investigate possible defocusing effects.

8.1 Modelling Approach

Although the performance of the line feed design was evaluated using an aperture efficiency analysis in Section 7.3, parameters such as reflector pattern half-power beamwidth, sidelobe levels and cross-polar levels can only be obtained using the combined feed and reflector analysis described in Chapter 5.

The technique begins by using the feed model developed in Section 5.5 to represent the measured radiation patterns presented in Section 7.2.1. This enables the measured pattern to be included in the reflector simulation. The feed model consists of a pair of current point sources which are symmetrically spaced at a height of around 0.25λ above the ground plane, at the centre frequency. For dual linear polarisation, the co- and cross-polar patterns correspond to either a TM or TE component analysis, as shown in Table 5.1. Hence, two feed models are required for each polarisation. Beam shaping channels are used in the TE model to improve its co-polar beamwidth match with the TM model, as described in Section 5.6.3. Measured vertical and horizontal polarisation co-polar patterns are represented using the corresponding TE or TM feed model by adjusting the spacing of the point sources above the ground plane to generate a pattern that matches the beamwidth of the measured pattern. Measured cross-polar patterns are more difficult to model because some patterns are asymmetric about 0° azimuth. These asymmetries are due to element construction and test range effects, which are not included in the feed model. At 0° scan angle, there is no cross-polar component assumed for the feed model because of the separation of the electromagnetic fields into TE and TM components. Cross-polar levels at 0° scan angle for the main beam are not modelled. Instead, they can be estimated by the measured scan element pattern in Figure 7.26 and are < -22 dB for both polarisations.

Measured cross-polar patterns at scan angles other than 0° (Figures 7.22 to 7.24) show a null at 0° azimuth angle. This characteristic was represented in the feed model by applying a 180° phase difference between the pair of current point sources. The beamwidth of the cross-polar lobes were modified to match those in the measured patterns, by adjusting the spacing between the sources. Because two separate programs are used to generate the TE and TM components for a particular polarisation, the scaling factor between the co- and cross-polar patterns was not included in the models. To account for this, scaling factors were applied for each co- and cross-polar pattern for the particular polarisation in the feed model by adjusting the magnitude of the current point sources such that the simulated patterns matched the measured patterns. Once the measured co- and cross-polar patterns were correctly modelled, the reflector pattern was obtained using a combined feed and reflector analysis, as described in Section 5.6. A comparison of the simulated patterns from the feed model with measured patterns, at 866 MHz for a 30° scan angle, is shown in Figure 8.1. Simulated reflector radiation patterns using the feed model are shown in Figure 8.2.

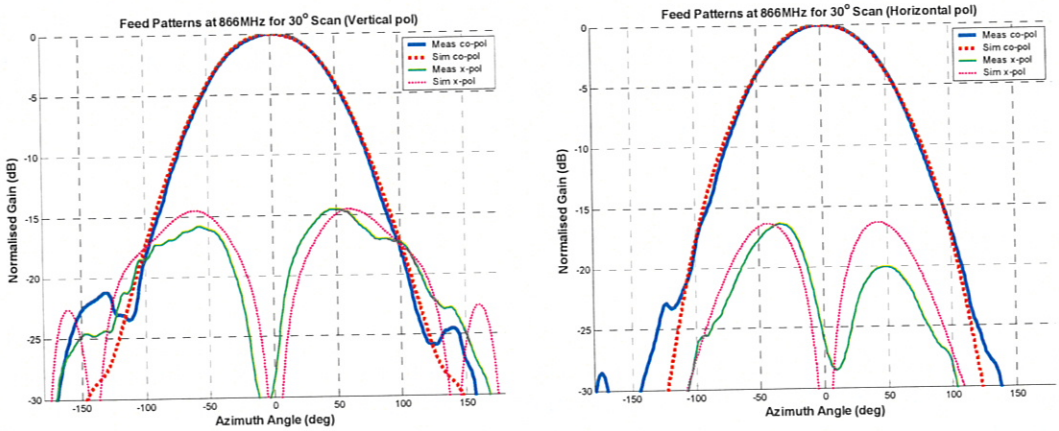

(a) (b)

Figure 8.1 Measured and simulated patterns from the TM and TE models at 866 MHz for 30° scan angle. (a) Vertical polarisation. (b) Horizontal polarisation.

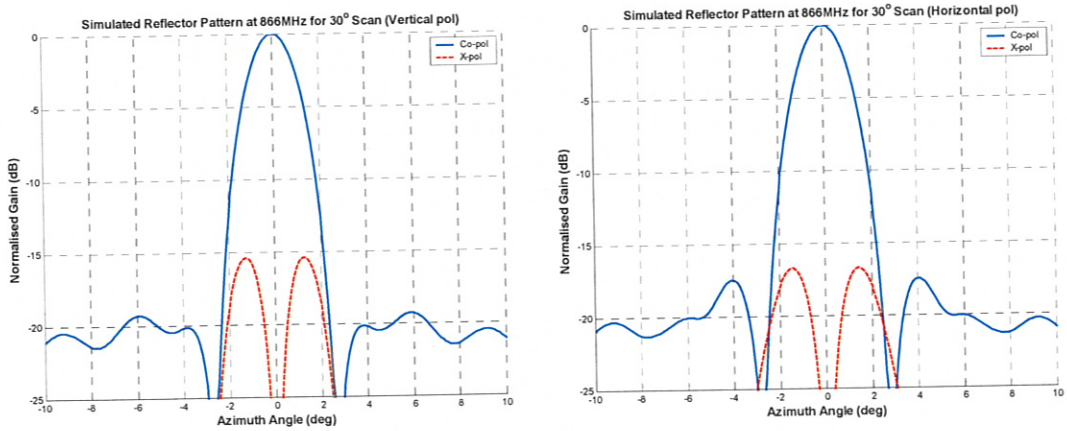

(a) (b)

Figure 8.2 Simulated reflector patterns using measured feed results at 866 MHz for 30° scan angle. (a) Vertical polarisation. (b) Horizontal polarisation.

Simulated co-polar feed patterns in Figure 8.1 show good agreement with measured patterns within an azimuth range of ±115°. However, simulated patterns in the back-

radiation region show an increased deviation from the measured patterns. As a result, estimating the noise temperature due to the line feed using the simulated reflector patterns could be inaccurate. The spillover temperature will be used to estimate the noise temperature because it is calculated directly from the measured feed patterns, as presented in Section 8.2. The simulated vertical polarisation cross-polar pattern shows good agreement with measurement. However, there is a 4 dB difference between simulated and measured cross-polar levels for the horizontal polarisation at an azimuth angle of 45° (Figure 8.1(b)), due to asymmetries. The simulated peak cross-polar level for the horizontal polarisation agrees with the measurement; which is the main result that determines the limiting cross-polar ratio (XPR) in the main beam. Simulated reflector patterns are different for vertical and horizontal polarisations, due to the different scattering characteristics of the respective polarisations (Figure 8.2).

The approach used to determine the reflector patterns assumes the feed performance degradation due to scanning effects is included in the element patterns. However, the gain variation due to a change in scan angle caused by the standing wave between the reflector vertex and ground plane is not included. There are also additional standing waves generated by the feed support struts, with two distinct spacings along the line feed direction, which vary with scan angle. These effects have not been investigated due to difficulty in producing an accurate model. Currently at the MOST all gain variations with scan angle, described in Section 2.5, are encapsulated in an East-West gain function (EWGF) measurement depicted in Figure 2.6. It is anticipated that the gain variation with scan angle will be determined experimentally once the new line feed is installed at the MOST. Therefore simulated reflector patterns in Section 8.2 do not include an analysis of the reflector gain. Because this thesis concentrates on the line feed development, only the gain variations from the feed have been investigated in detail. With the gain variation caused by feed mutual coupling presented in Section 7.2.2.

8.2 Reflector Simulations with Measured Patterns

A set of feed patterns was generated using the modelling approach described in Section 8.1 to match the measured patterns across a frequency range of 700–1100 MHz and a scan angle range of 15°–45°. Results for the half-power beamwidth, sidelobe level and cross-polar ratio (XPR) are shown respectively in Figures 8.3 to 8.5. The reflector XPR is specified as the maximum level in the angular region spanning the reflector half-power beamwidth. An estimate for the noise temperature due to line feed radiation is provided by the spillover temperature calculations shown in Figure 8.6.

Reflector beamwidths across the frequency range for the vertical polarisations vary from 1.5°–3.3°, whereas beamwidths for the horizontal polarisation vary from 1.7°–2.8°. The increased variation for the vertical polarisation can be explained from the wideband reflector performance simulations, at 0° scan angle, in Section 5.6.4. Figure 5.28 shows the reflector beamwidth across the 500–1000 MHz range with a periodic 50 MHz variation generated by the standing wave between the reflector vertex and feed ground plane. The vertical polarisation co-polar pattern, TM component in Figure 5.28(a), at 700 MHz corresponds to the location of a periodic maximum. For the horizontal co-polar pattern, corresponding to the TE component in Figure 5.28(b), at 700 MHz the beamwidth is located at a point in between the periodic maximum and minimum, which

produces a reduced beamwidth variation across the frequency range at 0° scan angle. In general, for both polarisations, the beamwidths at lower frequencies are larger due to the decreased electrical collecting area of the reflector which broadens the beamwidth. The converse is true for higher frequencies.

Although no experimentally measured reflector patterns using the new line feed are yet available, the simulated beamwidths at 866 MHz can be compared with the current MOST reflector beamwidth at 843 MHz, of 2.3°, as shown in Figure 2.7. Simulated reflector beamwidths using measured patterns of the new line feed for both vertical and horizontal polarisations at 866 MHz show similar beamwidths ~ 2.2° (Figure 8.3). Sidelobe levels across the frequency and scan angle range, in Figure 8.4, are < –15 dB for both polarisations. The XPR generally increases with scan angle for both polarisations due to the degradation in feed pattern cross-polar performance, as seen in Figure 8.5. This result signifies that the polarisation performance of the main reflector beam is dominated by the feed rather than the reflector or ground plane. Increased reflector pattern XPR levels for the vertical polarisation at large scan angles correspond to the increased feed polarisation degradation, as shown in Figure 7.24(a).

Spillover temperature for the vertical polarisation (Figure 8.6(a)) across the frequency and scan angle range varies from 3.5–6.0 K. Increased temperature occurs for the vertical polarisation at lower frequencies and large scan angles due to the increased cross-polar levels and the co-polar pattern broadening. Spillover temperatures for the horizontal polarisation (Figure 8.6(b)) vary from 3.5–4.0 K across the frequency and scan angle range. Spillover temperatures for the horizontal polarisation are less affected by a change in scan angle because the electric field orientation of the horizontal polarisation is not aligned with the scanning direction and mutual coupling effects are not as significant.

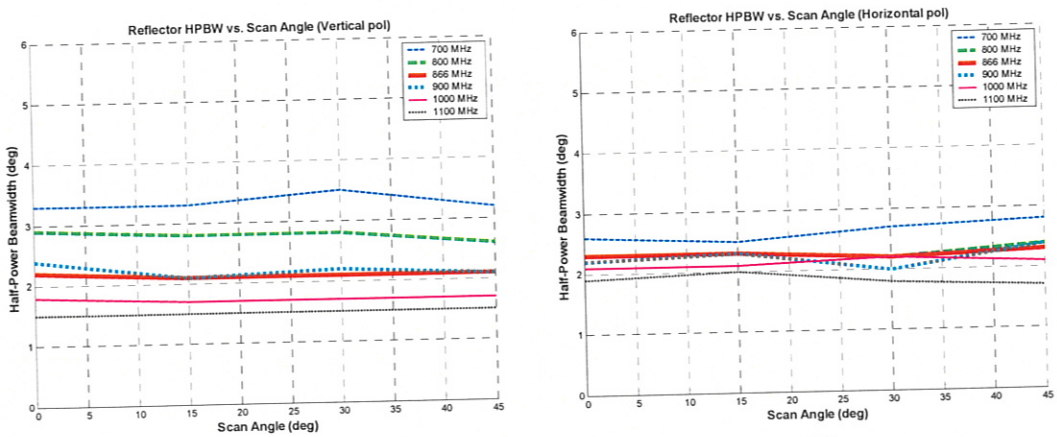

(a) (b)

Figure 8.3 Reflector half-power beamwidth vs. scan angle for measured feed patterns. (a) Vertical polarisation. (b) Horizontal polarisation.

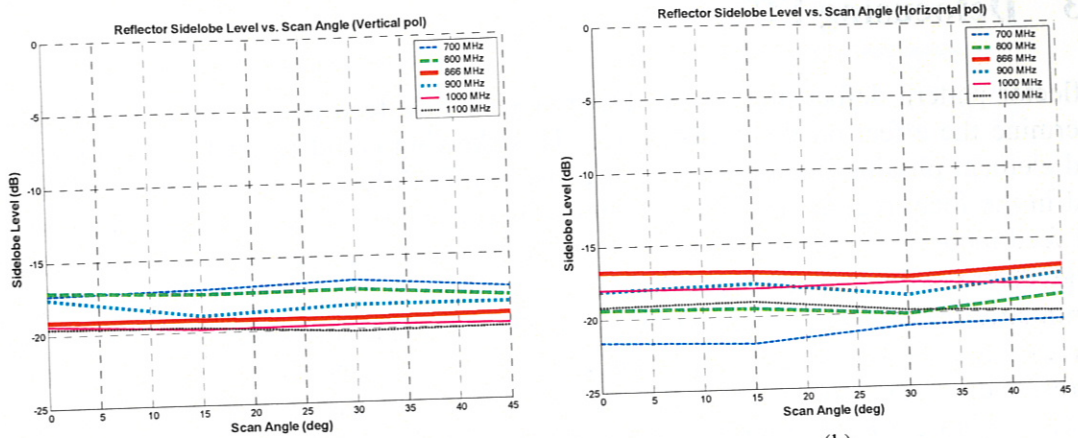

(a) (b)

Figure 8.4 Reflector sidelobe level vs. scan angle for measured feed patterns. (a) Vertical polarisation. (b) Horizontal polarisation.

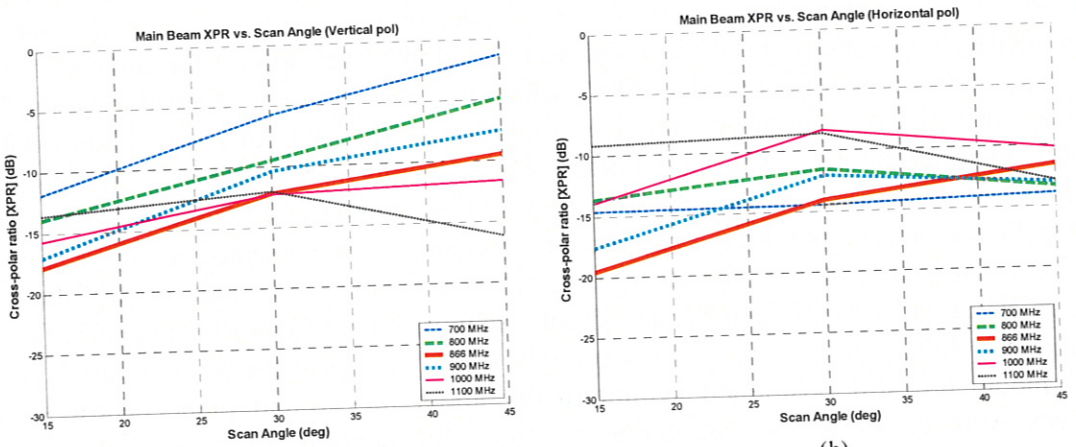

(a) (b)

Figure 8.5 Cross-polar ratio in the main beam of the reflector pattern. (a) Vertical polarisation. (b) Horizontal polarisation. (Note cross-polar feed model not defined for 0°).

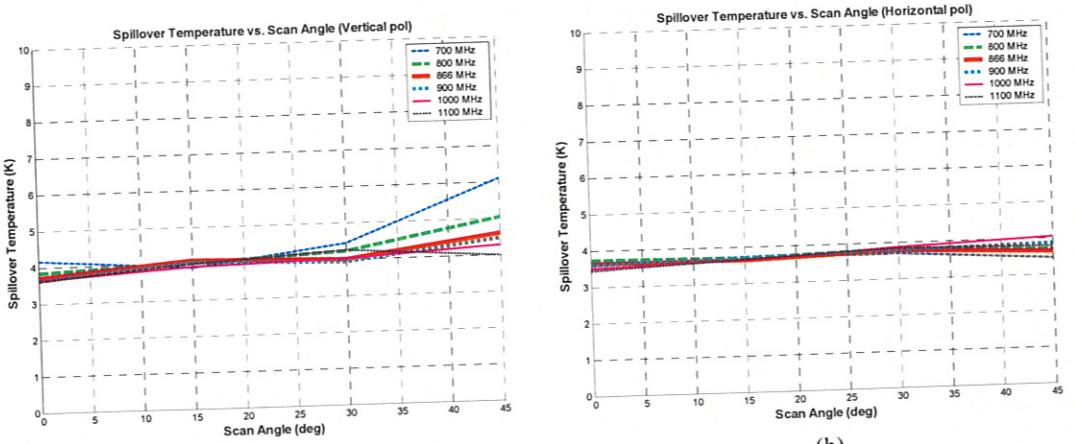

(a) (b)

Figure 8.6 Spillover temperature vs. scan angle across the 700–1100 MHz frequency range. (a) Vertical polarisation. (b) Horizontal polarisation.

8.3 Defocusing Effects

Reflector pattern defocusing caused by an asymmetric feed pattern was investigated to determine the effect on the performance. This skewing could result from incorrect line feed element phasing due to element or phase shifter failure or misalignment of the line feed in the focal region. The investigation was carried out at 866 MHz for the co-polar TM feed model, using two current point sources spaced symmetrically about the ground plane centre with the spacing adjusted to produce a feed beamwidth of 89°. The asymmetric pattern was generated by introducing a phase difference between the point sources. Figure 8.7 shows a comparison of the symmetric and asymmetric feed patterns. Corresponding reflector patterns for the symmetric and asymmetric feed patterns are shown in Figure 8.8, with the symmetric pattern represented by the solid curve and the asymmetric pattern represented by the dashed curve.

A comparison between symmetric and asymmetric feed for the reflector radiation performance is contained in Table 8.1. The reflector pattern in Figure 8.8(a) for the asymmetric feed pattern shows an increase in sidelobe level around the angular region corresponding to the reflector edge, +88°, which the feed pattern is skewed towards. The zoomed-in reflector pattern generated by the asymmetric feed pattern in Figure 8.8(b) shows sidelobes increase by around 3 dB, and beamwidths increase by 0.3°. Although the asymmetric feed pattern beam centre shifted +27° in azimuth, its reflector temperature and spillover temperature did not significantly increase. This is because the large taper of the MOST reflector corresponds to a large angular collecting area with most of the feed pattern captured by the reflector (±88° angular region). The reflector beam centre for the asymmetric feed pattern shifts only minimally (+0.1°) because the point sources in the feed model are still positioned symmetrically about the ground plane centre. If the sources were offset in the *y*-direction or along the aperture to create the reflector defocusing, as was investigated in Section 5.6.1, a larger beam centre shift and sidelobe levels would be generated.

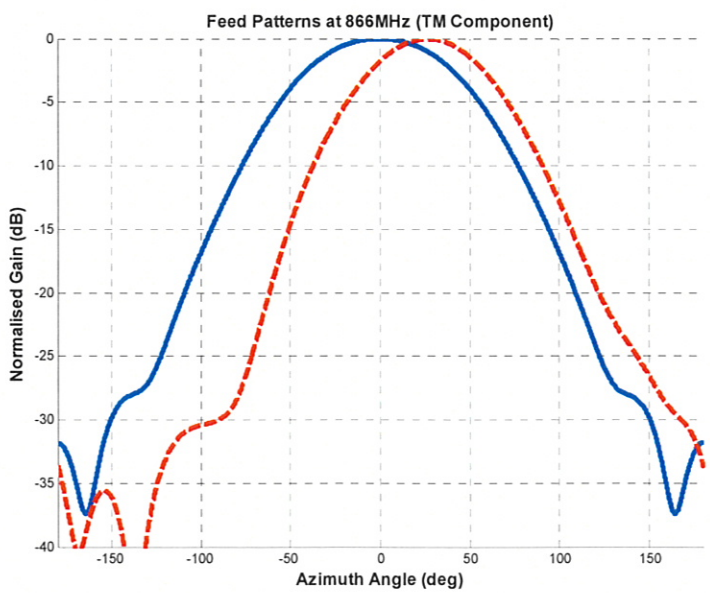

Figure 8.7 Feed patterns at 866 MHz for defocusing investigation: the solid-line is symmetric feed pattern and dotted line is asymmetric feed pattern.

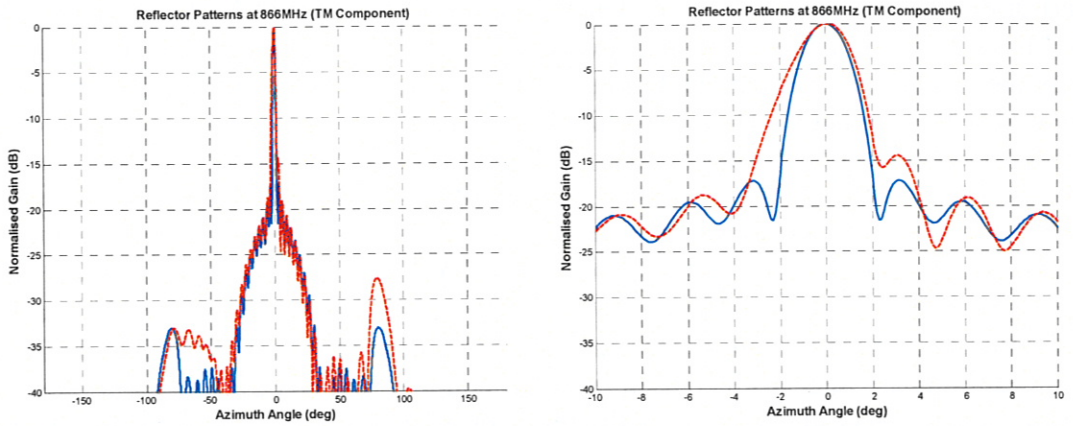

(a) (b)

Figure 8.8 Reflector patterns at 866 MHz for defocusing investigation, using feed patterns in Figure 8.7. (a) Full –180° to +180° range. (b) Zoomed in –10° to +10° range.

Parameter	Symmetric pattern	Asymmetric pattern
Feed HPBW (°)	89.0	70.0
Feed beam centre (°)	0.0	+27.0
Spillover efficiency	0.99	0.98
Taper efficiency	0.52	0.58
Spillover temperature (K)	3.6	4.0
Reflector HPBW (°)	1.9	2.2
Reflector beam centre (°)	0.0	+0.1
Reflector gain (dB)	19.5	19.0
Sidelobe level (dB)	17.0	14.0
Reflector temperature (K)	3.2	3.3

Table 8.1 Comparison of line feed/reflector parameters for symmetric and asymmetric feed patterns.

8.4 Summary

A methodology to obtain the reflector pattern from measured transverse feed patterns was described. This approach uses a feed model to synthesise simulated patterns that match the measured co- and cross-polar patterns, then the feed model is included in a reflector simulation to obtain the reflector pattern. Good agreement between the simulated and measured feed patterns was shown for angles within ±115° in azimuth. Because of the inaccuracy of the feed model in estimating the measured pattern in the back radiation direction, the reflector temperature was not calculated. Instead, the noise temperature was estimated by calculating the spillover temperature, which provided a more accurate result. The gain variation with scan angle caused by secondary scattering from support struts and ground plane blockage was not modelled at this stage. This variation can be measured as an East-West gain function, described in Section 2.5, once the new line feed is installed at the MOST.

Reflector simulations for the measured feed patterns were performed across a 700–1100 MHz frequency range and 0°–45° scan angle range. The simulated reflector beamwidth variation for the vertical polarisation was 1.5°–3.3° and was 1.7°–2.8° for the horizontal polarisation. The beamwidth narrowed at the higher frequency limit due to the increase in the electrical dimensions of the reflector and broadened at lower frequency limit as the

electrical dimensions decreased. Simulated beamwidths at 866 MHz for both polarisations were around 2.1°–2.3°, which is close to the current MOST beamwidth at 843 MHz, 2.3°. Simulated sidelobe levels for both polarisations remained < –15 dB across the frequency and scan angle range. The cross-polar ratio in the reflector pattern increased with scan angle. This result highlights that the cross-polar performance of the reflector pattern is dominated by the feed polarisation performance rather than the reflector or ground plane. Spillover temperatures estimate the amount of noise contribution from the measured line feed radiation. For the vertical polarisation, the spillover temperatures range from 3.5–6.0 K and for the horizontal polarisation range from 3.5–4.0 K. An increased spillover temperature limit occurs for the vertical polarisation because it has an increased back-radiation at the lower frequency limit and large scan angles due to increased mutual coupling. A feed defocusing analysis investigates the effect of illuminating the reflector with an asymmetric feed pattern. This scenario may be caused by instrumentation effects such as phase shifter or element failure or incorrect feed alignment. Simulations for the asymmetric feed pattern showed a minimal change in reflector noise temperature and beam centre position, as most of the feed radiation was captured by the MOST reflector. However, sidelobe levels and beamwidth levels were shown to increase.